

Postirradiation Examination of the ATF-1 Experiments – 2018 Status

Nuclear Technology Research and Development

**Jason M. Harp
Fabiola Cappia
Luca Capriotti**

***Prepared for
U.S. Department of Energy
Advanced Fuels Campaign***

***Idaho National Laboratory
September 2018***

NTRD-FUEL-2018-000054



DISCLAIMER

This information was prepared as an account of work sponsored by an agency of the U.S. Government. Neither the U.S. Government nor any agency thereof, nor any of their employees, makes any warranty, expressed or implied, or assumes any legal liability or responsibility for the accuracy, completeness, or usefulness, of any information, apparatus, product, or process disclosed, or represents that its use would not infringe privately owned rights. References herein to any specific commercial product, process, or service by trade name, trade mark, manufacturer, or otherwise, does not necessarily constitute or imply its endorsement, recommendation, or favoring by the U.S. Government or any agency thereof. The views and opinions of authors expressed herein do not necessarily state or reflect those of the U.S. Government or any agency thereof.

SUMMARY

The Advanced Fuels Campaign in collaboration with industry are working to develop enhanced accident tolerant fuels for light water reactors. The initial irradiations of these concepts were performed in the Idaho National Laboratory Advanced Test Reactor using simple drop-in style irradiations. These irradiations are collectively referred to as ATF-1. The postirradiation examination of ATF-1 has begun and some concepts have now completed initial examination. This report describes the results of examinations on ATF-1 irradiations designed to test the feasibility of enhancing UO_2 thermal conductivity with additives, ATF-1 irradiations of uranium silicide, and the current status of ATF-1 irradiations that are in process at the hot-cell.

Enhanced thermal conductivity uranium dioxide composites containing silicon carbide ($\text{UO}_2\text{-SiC}$) and diamond ($\text{UO}_2\text{-diamond}$) have been irradiated to low burnup. The conditions of this irradiation test and subsequent postirradiation examinations are discussed. These irradiations evaluate fuel microstructure and potential fuel cladding interaction under representative light water reactor power conditions. Both non-destructive and destructive techniques have been used to evaluate fuel integrity, fission gas release, fission product distribution, burnup, fuel swelling and cladding strain. Examination of the $\text{UO}_2\text{-SiC}$ pellets revealed enhanced cracking when compared to a UO_2 rodlet also irradiated under similar conditions. Additionally instability of the SiC whiskers in the uranium dioxide matrix was observed in the pellet central region, where the local temperatures exceeded 1300 °C. The microstructure of the diamond-added UO_2 was severely disrupted during irradiation, resulting in local migration of cesium along the fuel stack and increased fission gas release when compared with the expected release from the Vitanza curve at corresponding values of burnup and irradiation temperature. The postirradiation examination results cast doubt on the suitability of these additives to improve UO_2 fuel performance in a way that would lead to enhanced accident tolerance.

Additionally, postirradiation examination data of U_3Si_2 fuels at low burnup (i.e., < 20 GWd/tHM) for application in advanced Light Water Reactor (LWR) is presented. The U_3Si_2 pellets show limited cracking in comparison to the expected behavior of UO_2 at same power level. In addition, gamma scanning data did not reveal migration of fission products. Minor homogeneous hardening along the pellet radius due to accumulation of fission products and radiation damage was measured by microindentation. The fission gas release and swelling remains very low. Formation of fission gas bubbles resolvable with optical microscopy occurs from the pellets center outward to approximately 60% of the fuel pellet radius. The overall data suggest a good performance of this accident tolerant fuel candidate at low burnup.

Finally, the current status of postirradiation examination on other ATF-1 irradiations will be discussed. These irradiations include UO_2 clad in an FeCrAl alloy, an alternative uranium silicide compound U_3Si_5 also clad in a FeCrAl alloy, and an interaction test between UO_2 and different FeCrAl alloys.

INTENTIONALLY BLANK

CONTENTS

SUMMARY	iii
ACRONYMS	x
1. INTRODUCTION	1
2. Summary of Experiment and Irradiation Conditions	3
2.1 Experiment Test Matrix	3
2.2 Irradiation Capsule Design	4
2.3 Irradiation History	5
3. ATF-1A	7
3.1 Results from PIE	7
3.1.1 Neutron Radiography	7
3.1.2 Dimensional Inspection	9
3.1.3 Gamma Spectrometry	10
3.1.4 Fission Gas Release	11
3.1.5 Burnup	12
3.1.6 Optical Microscopy	12
3.2 Discussion	16
4. ATF-1W	20
4.1 Results from PIE	20
4.1.1 Neutron Radiography	20
4.1.2 Dimensional Inspection	22
4.1.3 Gamma Spectrometry	25
4.1.4 Fission Gas Release	27
4.1.5 Burnup	27
4.1.6 Optical Microscopy and Microhardness Testing	28
4.2 Discussion	33
4.2.1 As-Fabricated Microstructure Image Analysis	37
4.2.2 Irradiated Microstructure Image Analysis	41
5. Other ATF-1 PIE	46
5.1 ATF-18 ORNL LOCA FCA-L3	46
5.2 ATF-06, ATF-08, ATF-45, ATF-73	47
6. CONCLUSIONS	49
7. REFERENCES	50

FIGURES

Figure 1. BSE image of the as-fabricated microstructure [26] 4

Figure 2. (a) Cross section of the ATF-1 basket, capsule and rodlet, (b) Typical configuration of ATF-1 rodlet and capsule 4

Figure 3. Irradiation History of ATF-1A R1, R4, and R5..... 5

Figure 4. Irradiation History of ATF-1W R4 and R6 6

Figure 5. Thermal neutron radiography image of the three rodlets. From left to right: UO₂ (R1), UO₂-SiC (R4) and UO₂-diamond (R5). 8

Figure 6. Neutron radiography of ATF-1A rodlets after capsule disassembly (left) thermal (right) epithermal 9

Figure 7. Measurement of fuel rod diameter along the rodlet axial length for the three rods. For each axial location, error bars represent 95% confidence interval of the mean value calculated over seven different orientations. The purple line represents the nominal as-fabricated diameter value..... 10

Figure 8. Axial gamma scanning of ¹³⁷Cs for (a) R1, (b) R4 and (c) R5 (black, solid lines). In (a)-(b) the calculated axial burnup profile is also shown (dashed line). 11

Figure 9. (a) Low magnification ceramography cross section of R1. (b) High magnification image of the inner part of the pellet ($r/r_0 < 0.3$). Red circle highlights the grain boundary covered by fission gas bubbles. (c) High magnification image of the external part of the pellet ($r/r_0 > 0.3$). 13

Figure 10. (a) Low magnification ceramography cross section of R4. (b) High magnification image of the inner part of the pellet ($r/r_0 < 0.32$). (c) High magnification image of the external part of the pellet ($r/r_0 > 0.32$) 14

Figure 11. Low magnification (50x) ceramography samples of R5 showing a (a) radial cross section and a (b) longitudinal section. (c) High magnification image (1000x) highlighting the cracked pellet matrix 15

Figure 12: Radial profile temperatures for (a) R1, (b) R4 and (c) R5. Circles: maximum Linear Heat Generation Rate (LHGR). Squares: average LHGR, Triangles: minimum LHGR..... 17

Figure 13: Porosity radial profile for rod R1 (black dots). Average as-fabricated porosity value (red solid line). 18

Figure 14. (a)-(b) Result of the application of the standard deviation filter to the low magnification images of R1 and R4, respectively. Resulting final segmentation of the pellet central region based on the algorithm. (c) R1, (d) R4 19

Figure 15. Capsule neutron radiographs of the ATF-1W R4 and R6 21

Figure 16. Rodlet neutron radiography of ATF-1W rodlets (a) thermal (b) epithermal 22

Figure 17. Dimensional measurements of ATF-1W R4. The measured value represent the average of measurements taken every 5°. Red solid lines indicate the nominal values..... 23

Figure 18. Dimensional inspection of ATF-1W R4 showing the probes at the 0 Position of Figure 17..... 24

Figure 19. Dimensional measurements of R6. The measured value represent the average of measurements taken every 5°. Red solid lines indicate the nominal values. 25

Figure 20. Axial distribution of select gamma emitting radionuclides in ATF-1W R6.....	26
Figure 21. Two-dimensional gamma spectrometry of major radionuclides for (a) R4 and (b) R6.....	27
Figure 22. Low magnification (50x) ceramography cross section of (a) R4 and (b) R6.	29
Figure 23. High magnification images of the irradiated microstructure from rodlet (a)-(c) R4 and (d)-(f) R6. The dashed circles in Fig. 12f indicate very tiny fission gas bubbles.	30
Figure 24. Radial profile of the microhardness for the two irradiated rods. The average microhardness of unirradiated U_3Si_2 [15] is also reported in red.	31
Figure 25. Indentation imprints. (a), (c): bright field microscopy; (b), (d): DIC microscopy. Magnification: 500X.....	32
Figure 26. Indentation imprint showing edge spallation. (a): bright field microscopy; (b): DIC microscopy. The use of DIC images highlights partial sink in of the surface next to the indentation. Magnification: 500X.....	32
Figure 27. Indentation imprint showing slip lines parallel to the imprint edges. (a): bright field microscopy; (b): DIC microscopy. Magnification: 500X.....	33
Figure 28: Measured number of pellet fragments from ceramography cross sections of U_3Si_2 fuels (black dots). Expected number of fragments in UO_2 pellets as a function of the average LHGR [51].....	34
Figure 29. Empirical cumulative distribution function of the UO_2 precipitate area in the as-fabricated microstructure.	35
Figure 30. Radial distribution of the UO_2 precipitates and associated porosity for the two irradiated rodlets.	36
Figure 31. Radial distribution of fission gas bubbles for the two irradiated rodlets.	37
Figure 32. Algorithm scheme for the as-fabricated microstructure.	39
Figure 33. (a) Initial porosity segmentation, (b) pore refinement based on region merging via color-merging and edge smoothing.	39
Figure 34. (a) Original BSE image, (b) initial segmentation using a k-means algorithm with 4 clusters, (c) final output of the segmentation after optimization in STEP 2 and 3.	40
Figure 35. (a) Texture score transform of the original image, (b) Segmentation of the borders based on a 3-cluster classification of the score in (a).	41
Figure 36. Algorithm scheme for the irradiated microstructure.	43
Figure 37. (a) Original image, (b) Segmentation results overlayed to the original image in (a). Red color corresponds to the UO_2 precipitates, black color to the porosity and green color to the fission gas bubbles.	44
Figure 38. Examples of different configurations of UO_2 precipitates and associated porosity encountered in the images: (a) Case 1, (b) Case 2, (c) Case 3.....	45
Figure 39. Logic tree to separate the UO_2 precipitates from the internal porosity performed in STEP 1 phase B.	45
Figure 40. Visual Examination and neutron radiography of the ORNL LOCA FCA-L3 rodlet with a neutron radiography detail that shows cracking in the UO_2 pellets.....	46
Figure 41. Dimensional inspection of the FeCrAl rodlet from ATF-18 (ORNL LOCA FCA-L3)	47

Figure 42. Neutron radiography of ATF-1 capsules, from left to right ATF-06, ATF-08, ATF.45, ATF-73	48
--	----

TABLES

Table 1. ATF-1 Test matrix for ATF-1 rodlets that have begun PIE.....	3
Table 2: Irradiation data for the ATF-1A rodlets.....	12
Table 3: Quantitative image analysis results for the as-fabricated U ₃ Si ₂ microstructure.....	20
Table 4: Irradiation data for the ATF-1W rodlets.....	27

INTENTIONALLY BLANK

ACRONYMS

AFC	Advanced Fuels Campaign
AL	Analytical Laboratory
ASTM	American Society for Testing and Materials
ATF	Accident Tolerant Fuel
ATR	Advanced Test Reactor
BSE	Backscattered Electron
DIC	differential interference contrast
DOE	Department of Energy
EDX	energy-dispersive X-ray spectroscopy
FCCI	Fuel-cladding Chemical Interaction
FGR	Fission Gas Release
FIB	Focused Ion Beam
FIMA	<u>F</u> issions per <u>I</u> nitial heavy <u>M</u> etal <u>A</u> toms
GASR	Gas Assay, Sample, and Recharge
GECT	Gamma Emission Computed Tomography
HFEF	Hot Fuel Examination Facility
HPRR	High Performance Research Reactor
ICP-MS	Inductively Coupled Plasma, Mass Spectrometry
INL	Idaho National Laboratory
LBP	Local Binary Pattern
LHGR	Linear Heat Generation Rate
LOCA	Loss of Coolant Accident
LWR	Light Water Reactor
MCNP	Monte Carlo N-Particle
NRAD	<u>N</u> eutron <u>R</u> adiography Reactor
PGS	Precision Gamma Scanner
PICT	Peak Inner Cladding Temperature
PIE	Postirradiation Examination
PGS	Precision Gamma Scanner
PWR	Pressurized Water Reactor
RGB	red-gray-blue (monitor)
SE	secondary electron
SEM	Scanning Electron Microscope

TD	theoretical density
TEM	Transmission Electron Microscope
TRIGA	training, research, and isotope reactor (built by GA)
XRD	X-Ray Diffraction

INTENTIONALLY BLANK

POSTIRRADIATION EXAMINATION OF THE ATF-1 EXPERIMENTS – 2018 STATUS

1. INTRODUCTION

A goal of the Accident Tolerant Fuels (ATF) Campaign (ATF Campaign) is to accelerate the development of new fuels and cladding for current and future generations of Light Water Reactors (LWRs) with enhanced performance compared to the standard UO_2 -zircaloy system, in particular under severe accident conditions such as those involving loss of cooling [1]. The ATF candidates should be necessarily be able to: (1) maintain or improve current standards of fuel safety and reliability under normal LWR operating conditions; (2) undergo slower reaction kinetics with steam and lower generation rate of hydrogen or other combustible gases under accidental scenarios; (3) delay fission product release and fuel meltdown; (4) assure coolability of fuel assembly and its integrity as long as possible. Evaluation metrics span over all aspects of the fuel cycle, including eases of fabrication and manufacturability, impact on plant economics, operations, safety, back-end of the fuel cycle and environment [2]. A comprehensive overview of the campaign strategy and timeline is provided in Reference [1]. The scope of phase one of the ATF Campaign is to perform feasibility assessments of the new concepts to down select the most promising ones for further development during the subsequent phases. To facilitate this decision process a series of irradiations referred to as the ATF-1 irradiations has been initiated. As part of the “proof-of-concept” stage, preliminary irradiation of rodlets with radial dimensions prototypical of LWR commercial rods has been performed in drop-in capsules in the Advanced Test Reactor (ATR) at Idaho National Laboratory (INL). The focus of this test series is the determination of basic irradiation performance under normal LWR operating conditions, in order to provide early screening of the proposed concepts. During the ATF-1 irradiation, fuel and cladding were placed in an outer capsule that provides isolation from the ATR reactor water coolant and acts as the primary safety barrier in case of cladding failure. With this configuration, the test is designed to focus on fuel pellet performance and assess eventual fuel-cladding interaction, but not to evaluate the interaction of the cladding with reactor coolant. A summary of the ATF-1 irradiation device design is presented in Section 2 along with the irradiation histories for the ATF-1 capsules that have completed initial postirradiation examination (PIE).

Both revolutionary and evolutionary concepts are being considered within the ATF Campaign. While in the first case, completely new fuel systems are explored (e.g., uranium silicide, either FrCrAl or SiC cladding to mention some), in the other case, UO_2 with improved properties is studied. Thermal conductivity is certainly one of the thermophysical properties of primary interest, due to the crucial role it plays in all aspects of fuel performance and safety. The low thermal conductivity of UO_2 is a main drawback of the current LWR fuels, as it implies large radial thermal gradients and is one of the factors limiting the linear heat generation rate [3]. Enhanced thermal conductivity would provide benefits not only during accidental scenarios, but also during normal in-reactor operation [4,5]. At constant power, an increase in the fuel thermal conductivity will reduce the peak fuel and cladding temperature, which are important safety criteria [5]. Conversely, at constant peak temperature, the power density could be increased [6]. Enhancement of the fuel thermal conductivity via incorporation of highly thermally conductive secondary phases has long been pursued [7]. Recently, fabrication of high density UO_2 - SiC and UO_2 -diamond composite fuel pellets by spark plasma sintering has been proved successful on laboratory scale [8]. SiC has long been considered a primary candidate for nuclear fuel systems thanks to its favorable properties such as low neutron absorption cross section, oxidation and irradiation resistance, high melting temperature, and high thermal conductivity. It has been shown that addition of 10 vol% silicon carbide fibers to the UO_2 matrix could lead to an increase in thermal conductivity between 54.9% and 62.1%, as compared to the UO_2 values, when temperature is in the range 100 °C to 900 °C [9]. Diamond is an attractive candidate as nuclear fuel additive, since it is one of the best thermal conductors known [10] and has good radiation resistance [11]. Composites containing 3 μm diamond particles

showed the highest increase in the thermal conductivity, between 34.2% and 41.6% in the range 100 °C to 900 °C, according to laser flash measurements by Chen et al. [12]. These two types of composites have been tested in order to gather performance data for the early screening. Section 3 describes the PIE results of these fuels.

Uranium silicide compounds have been studied as potential nuclear fuels since the 1960s, in particular for application in research reactors. In the last years uranium silicides and, in particular, U_3Si_2 have received renewed attention as they have been proposed as potential accident tolerant fuels within the ATF Campaign [13]. The high thermal conductivity of U_3Si_2 and the increased uranium density in comparison to UO_2 make this compound a very attractive candidate. The higher thermal conductivity would imply a reduction in the stored thermal energy in the fuel, which is a critical factor during Loss of Coolant Accident (LOCA) [4,5]. The higher uranium loading would allow either to reduce the initial enrichment or to deploy cladding materials with increased neutronic penalty without the necessity to increase the enrichment. As part of the fuel development and qualification objectives, data regarding performance under irradiation are essential. Extensive literature documenting U_3Si_2 irradiation behavior is available at temperatures below 250 °C [14–19]. LWR fuels are typically irradiated at temperatures exceeding 300 °C, providing an irradiation environment substantially different from test reactor ones. Therefore, data from previous irradiation campaigns have limited applicability to the assessment of U_3Si_2 performance under commercial LWR conditions. For instance, recent ion-irradiation experiments have shown that the amorphization observed in research reactor U_3Si_2 fuels at doses below 0.3 dpa [17] does not take place above ≈ 240 °C [20], and U_3Si_2 retains its tetragonal crystalline structure up to 500 dpa at 600 °C [21]. Further studies have been performed to evaluate critical aspects of U_3Si_2 performance, such as bubble formation and grain subdivision by means of ion irradiation [22–24]. In-situ Transmission Electron Microscope (TEM) [24] confirmed U_3Si_2 amorphization-resistance at 350 °C, but highlighted that this material experiences polygonization and grain subdivision at doses as low as 0.8 dpa, with possibility of rim structure formation as in UO_2 .

Regarding the fission gas behavior, TEM analysis highlighted retention of the majority of the implanted Xe, with formation of dense distribution of small lattice intragranular and intergranular bubbles in the proximity of grain boundaries and irradiation-induced dislocations. The average size of both bubble populations remains below 10 nm, suggesting a limited swelling for burnups corresponding to 6% FIMA [23]. Integral neutron irradiation tests are fundamental to confirm these observations during in-reactor operation. For this purposes, U_3Si_2 pellets have been irradiated in the ATR at INL as part of the feasibility phase of the ATF Campaign (ATF-1). The goal of this first irradiation test is to assess the performance of U_3Si_2 in normal conditions. The PIE results are presented in Section 4.

2. Summary of Experiment and Irradiation Conditions

2.1 Experiment Test Matrix

The ATF-1 tests are designed to screen ATF concepts prior to full scale test irradiations in a test reactor water loop or in commercial reactors. The ATF-1 capsule tests a fuel compound (UO_2 , U_3Si_2) against a cladding material, and it is useful for investigating fuel cladding interaction and general fuel compound irradiation performance. The UO_2 additives test was sponsored by Framatome (formerly Areva) and are collectively referred to as ATF-1A in this report, and this nomenclature was used in the identifying marks on the rodlets. The U_3Si_2 test was sponsored by Westinghouse and is collectively referred to as ATF-1W in this test, and this nomenclature was used in the identifying marks on the rodlets. The ATF-1 rodlets that have been through or initiated PIE are shown in Table 1.

The ATF-1A experiments are meant to explore the performance of UO_2 composites. In addition to the UO_2 composites, UO_2 pellets were also fabricated at University of Florida [8] and were irradiated in the same type of capsule as the composite fuels. This rodlet provides the baseline against which the performance of the other fuels could be compared. Regarding the composites, the SiC and diamond content were 3.16 ± 0.32 wt% and 3.44 ± 0.34 wt% respectively. All the pellets were fabricated using spark plasma sintering, with an initial density of 96.5% theoretical density (TD) for UO_2 , 94.4% TD for the UO_2 -SiC composite and 95.3% TD for the other diamond-added pellets [8]. The fuel rodlets were assembled at INL. All rodlets had Zircaloy-4 cladding and were filled with helium. The rodlets were placed in stainless steels capsules in order to prevent fission product release to the reactor circuit in case of cladding failure. The helium filled gap between the rodlet and the capsule also establishes the proper cladding temperature conditions in the experiment.

For the ATF-1W irradiations, the U_3Si_2 pellets were produced at INL [25]. Detailed characterization of the starting material and the fabrication methodology can be found in references [25,26]. Figure 1 reports an example of the as-fabricated microstructure, indicating the nature of the impurities in this fuel. Six rodlets were assembled by stacking twelve enriched pellets (initial enrichment 5.44 wt% of U-235) in Zirlo cladding. The active fuel stack was topped with two depleted pellets which were drilled to accommodate melt wires for temperature monitoring purposes. An additional depleted pellet was located below the stack of enriched pellets. The rodlets were encapsulated in an outer stainless steel drop-in

Table 1. ATF-1 Test matrix for ATF-1 rodlets that have begun PIE

Rodlet ID	Capsule ID	Concept Lead	Fuel Material	Cladding Material
ATF-1A R1	ATF-00	Framatome	UO_2	Zircaloy-4
ATF-1A R4	ATF-03	Framatome	$\text{UO}_2 + \text{SiC}$	Zircaloy-4
ATF-1A R5	ATF-04	Framatome	$\text{UO}_2 + \text{Diamond}$	Zircaloy-4
ATF-1W R4	ATF-13	Westinghouse	U_3Si_2	Zirlo
ATF-1W R6	ATF-15	Westinghouse	U_3Si_2	Zirlo
LOCA-1	ATF-18	ORNL	UO_2	FeCrAl Alloy
FCCI-1	ATF-73	ORNL	UO_2	FeCrAl Alloy
ATF-1G R1	ATF-06	GE	UO_2	Alloy 33 (FeCrAl)
ATF-G R3	ATF-08	GE	UO_2	APMT (FeCrAl)
LANL-3	ATF-45	LANL	U_3Si_5	Kanthal-AF (FeCrAl)

capsules to avoid contamination of the coolant circuit in case of cladding failure and to provide the proper thermal conditions. Two rodlets (R4 and R6) have underwent PIE so far.

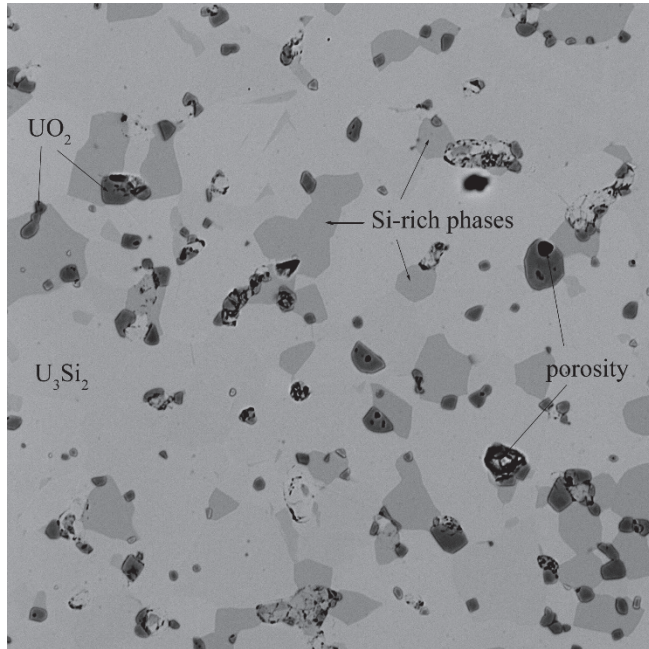


Figure 1. BSE image of the as-fabricated microstructure [26]

2.2 Irradiation Capsule Design

The ATF-1 rodlet basic design is to replicate a small section of a pressurized water reactor (PWR) fuel pin. The ATF-1 irradiation is a drop-in style ATR irradiation experiment [27,28]. The ATF-1 design consists of a fueled rodlet (fuel plus cladding) that is encapsulated in a stainless steel capsule. Drop-in tests use the heat generated from fission and gamma heating in the experiment and a temperature control gap between the rodlet and the capsule to maintain temperature. No active control mechanisms exist in drop-in designs. The typical design of an ATF-1 experiment is shown in Figure 2.

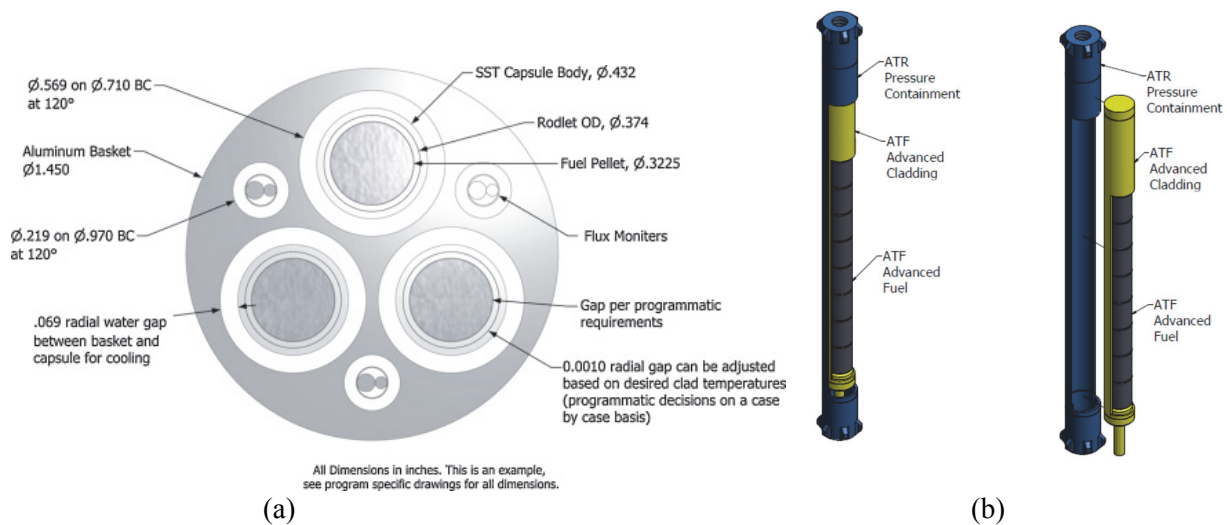


Figure 2. (a) Cross section of the ATF-1 basket, capsule and rodlet, (b) Typical configuration of ATF-1 rodlet and capsule

2.3 Irradiation History

The irradiation history of all ATF-1 capsules is recorded in Reference [29]. Similar reports that summarize the simulations of the ATF-1 capsules under irradiation are planned at the end of each fiscal year. The as-run neutronic and thermal irradiation histories for each rodlet were calculated by combining the results of neutronic and thermal analysis of each capsule. The heat generation and linear heat generation rate (LHGR) in each capsule is calculated using whole ATR core Monte Carlo n-Particle (MCNP 6.0) simulations coupled with ORIGEN for depletion. The recorded ATR power history from each cycle and the initial ATR core loading are used as inputs to these simulations. The heat generation rates are then supplied to a finite element analysis code (Abaqus) to calculate the temperatures in the capsule. The axial variation in power and temperature is relatively low, so only maximum temperatures are reported here. For the UO₂ fuel in ATF-1A, fuel performance can largely be tied back to LHGR and fuel centerline temperature. The histories of these metrics are plotted in Figure 3 for the 3 ATF-1A rodlets that have completed PIE. For U₃Si₂ it is less clear what metrics best illustrate fuel performance. In Figure 4, the LHGR, Peak Inner Cladding Temperature (PICT), and fuel centerline temperature histories are recorded for ATF-1W R4 and R6.

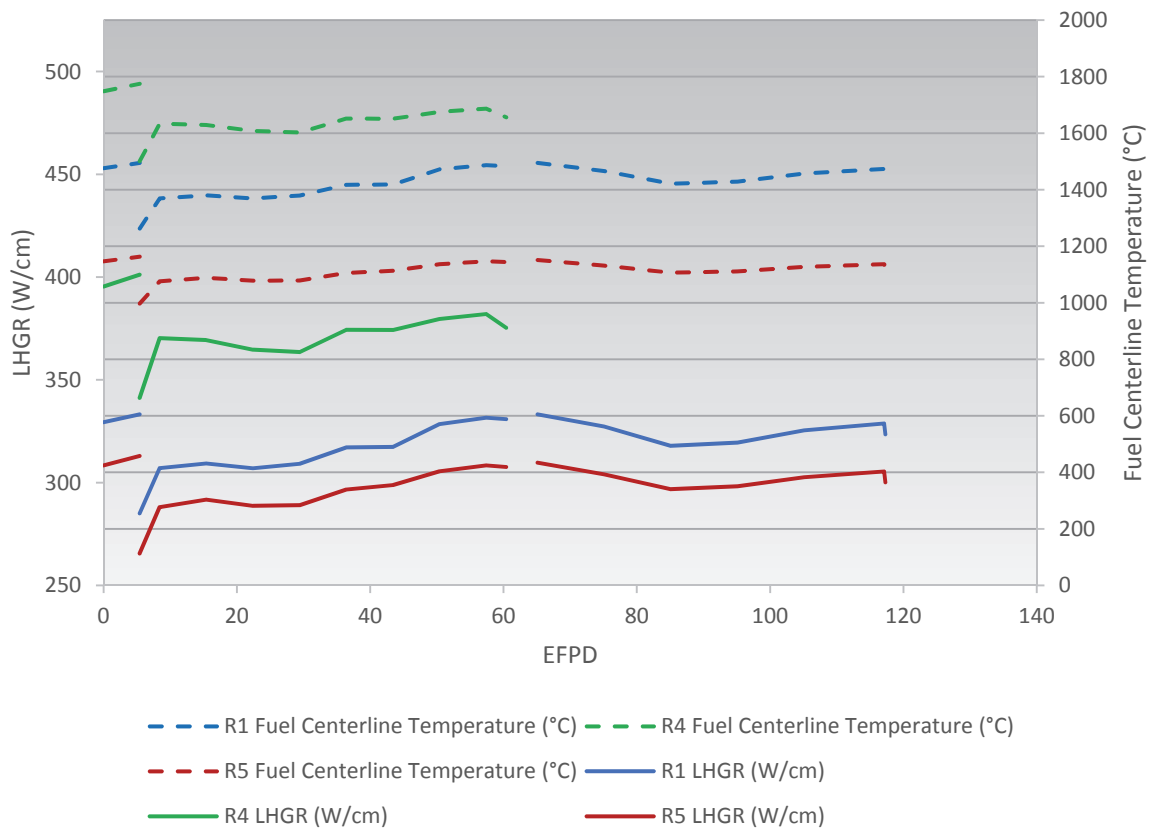


Figure 3. Irradiation History of ATF-1A R1, R4, and R5

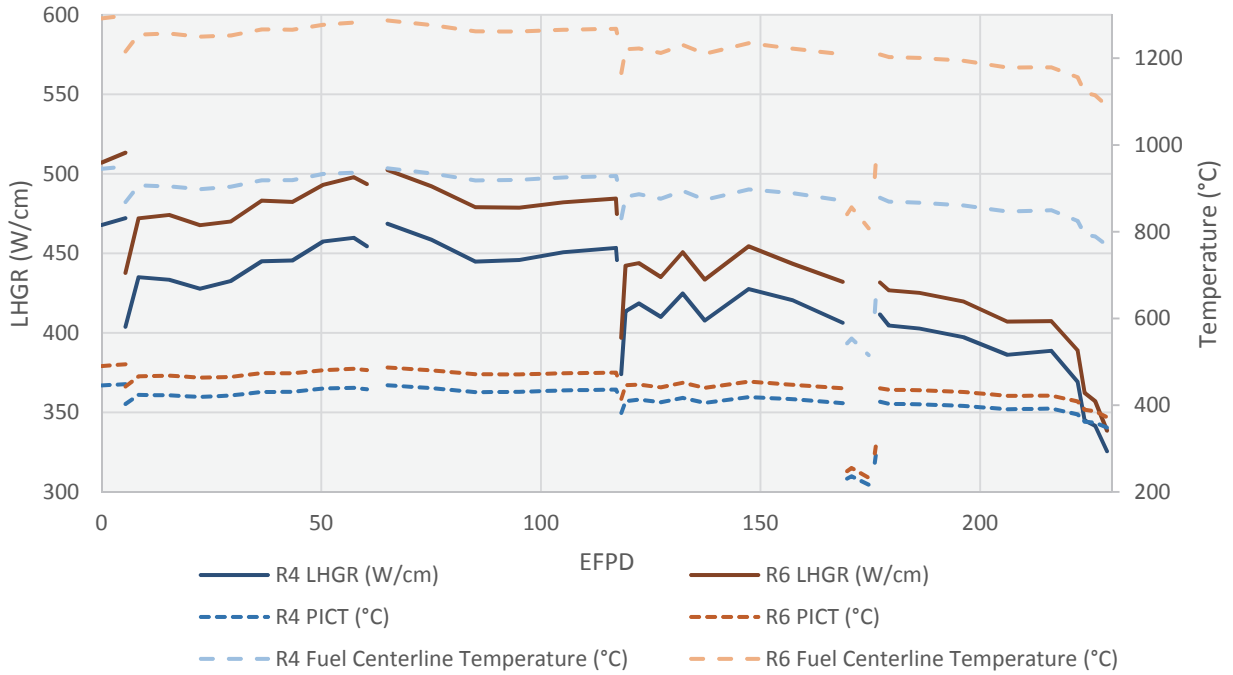


Figure 4. Irradiation History of ATF-1W R4 and R6

3. ATF-1A

After the rodlets were irradiated at the ATR, PIE was performed at the INL Hot Fuel Examination Facility (HFEF). Baseline non-destructive PIE performed on the rodlets included neutron radiography, gamma spectrometry, and dimensional inspection. Neutron radiography is performed using a small TRIGA reactor in the basement of HFEF. Radiographs are produced by placing the fuel in the neutron beam in front of a Dy foil for thermal neutron radiographs and a Cd-covered In foil for epithermal neutron radiographs. The images from the foils are then transferred to film, developed and scanned for examination [30]. The axial distribution of fission and activation products is collected with a hot cell gamma spectrometer, stage and collimator system [31]. Dimensional inspection is carried out using Sony Magnescale contact probes with a thickness uncertainty of $\pm 5 \mu\text{m}$. In addition, fission gas release measurements were conducted using the Gas Assay Sample and Recharge (GASR) system [32]. The collected gas was analyzed using gas mass spectrometry. Fuel pellet samples were cut from the middle of the active fuel length to perform chemical burnup analysis using wet chemistry and mass spectrometry methods by the "Fission Product Monitor - Residual Heavy Atom" technique [33]. The burnup sample was taken from the bottom part of the fourth enriched pellet, starting the count from the top of the fuel column. Optical microscopy was also performed on a transverse sample taken near the burnup sample and a longitudinal section if possible.

3.1 Results from PIE

PIE begins when the capsules enter the HFEF hot-cell. Prior to removing the rodlets from the capsules, visual exams, neutron radiography, and axially resolved gamma spectrometry are performed on the intact rodlets. In ATF-1A, there were no indications of any severe issues with the fuel performance. The rodlets were removed from the capsules and PIE on the rodlets began. Visual inspection was performed on the rodlets and no unusual features were detected.

3.1.1 Neutron Radiography

Neutron radiography was performed using the Neutron Radiography Reactor (NRAD) located in the basement of HFEF. The NRAD reactor is a 250kW TRIGA reactor with two beam lines. The east beam line services a position below the main floor of the hot cell and is used for irradiated fuel. Neutrons pass through the fuel specimen and expose different activation foils [30]. The radiography fixture contains a scale marked with Gd paint that produces a calibrated scale for quantitative measurements of irradiated fuel dimensions. The fixture used in these shots also contained a hafnium step wedge. This allows the gray scale from radiographs to be mapped to a known neutron attenuation.

Figure 5 reports the thermal neutron radiograph of the three rodlets while they were still in their capsules. The sharpness of this radiograph is superior to the later radiographs taken after removal from the capsule, and it is shown to demonstrate the typical information present in the radiographs. Capsule neutron radiographs were taken at an initial orientation and then at a rotation of approximately 90° from the original orientation. The radiographs taken after removal from the capsule were taken every 30° to 150° from the original orientation. Rodlet neutron radiographs are shown in Figure 6. There are some notable features in the radiographs. Cracking in individual pellets can be observed. It is also possible to see the dishing and chamfering fabricated into these pellets. It should also be noted that the fuel stack in R4 was less when fabricated than the other rodlets due to issues with adequate pellet supply.

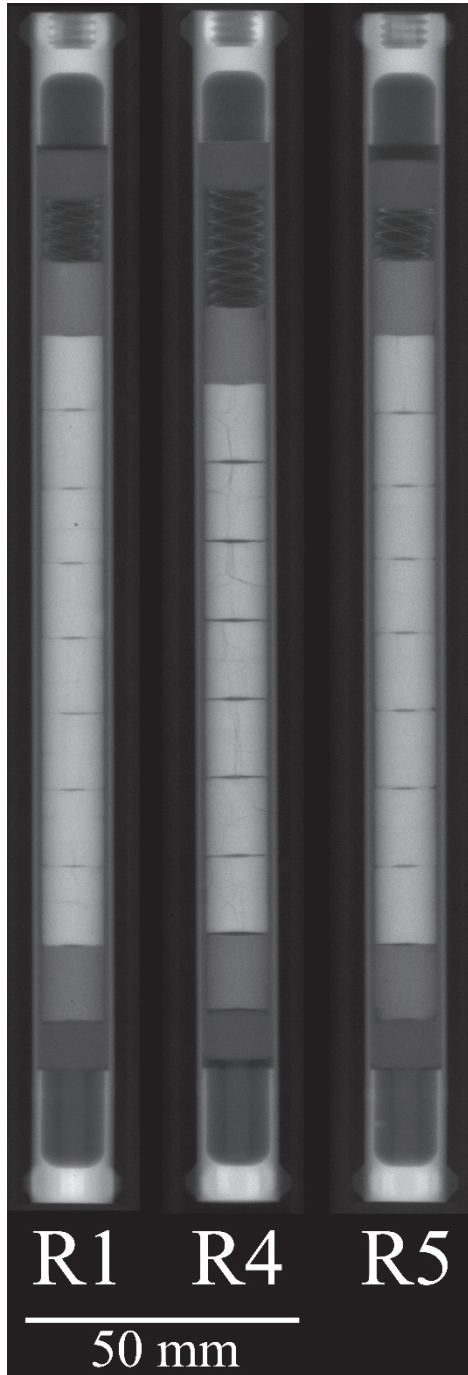


Figure 5. Thermal neutron radiography image of the three rodlets. From left to right: UO_2 (R1), $\text{UO}_2\text{-SiC}$ (R4) and $\text{UO}_2\text{-diamond}$ (R5).

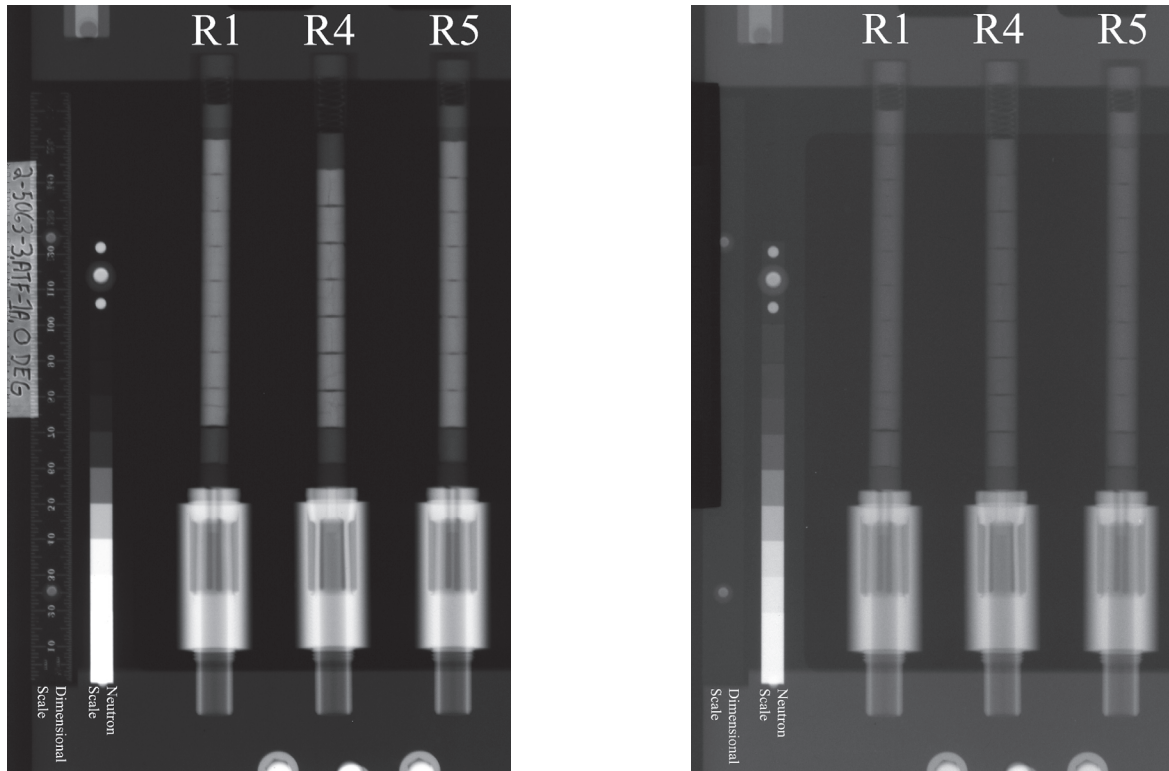


Figure 6. Neutron radiography of ATF-1A rodlets after capsule disassembly (left) thermal (right) epithermal

3.1.2 Dimensional Inspection

Dimensional inspections of ATF-1A were performed using the US HPRR Plate checker in HFEF. Outside diameter measurements were collected all along the rodlets in roughly 0.5 mm increments and at 7 angles every 30° from the initial scan angle to 180°. Diameter measurements are collected with $\pm 5 \mu\text{m}$ accuracy. The angle averaged measured diameters for the ATF-1A rodlets is shown in Figure 7. The specified cladding dimension is also shown. The diameters are plotted by the distance from the top of the fuel pin which puts the fueled portion of the rodlet towards the left side of the figure. The peak on the left side of the figure is the weld on the endcap. No significant radial strain of the cladding resulting in excessive diametral change of the pins was detected during dimensional analysis. The diameter value, when including the experimental uncertainty, is close to the nominal one along the entire rod axial length in all three cases (Figure 7).

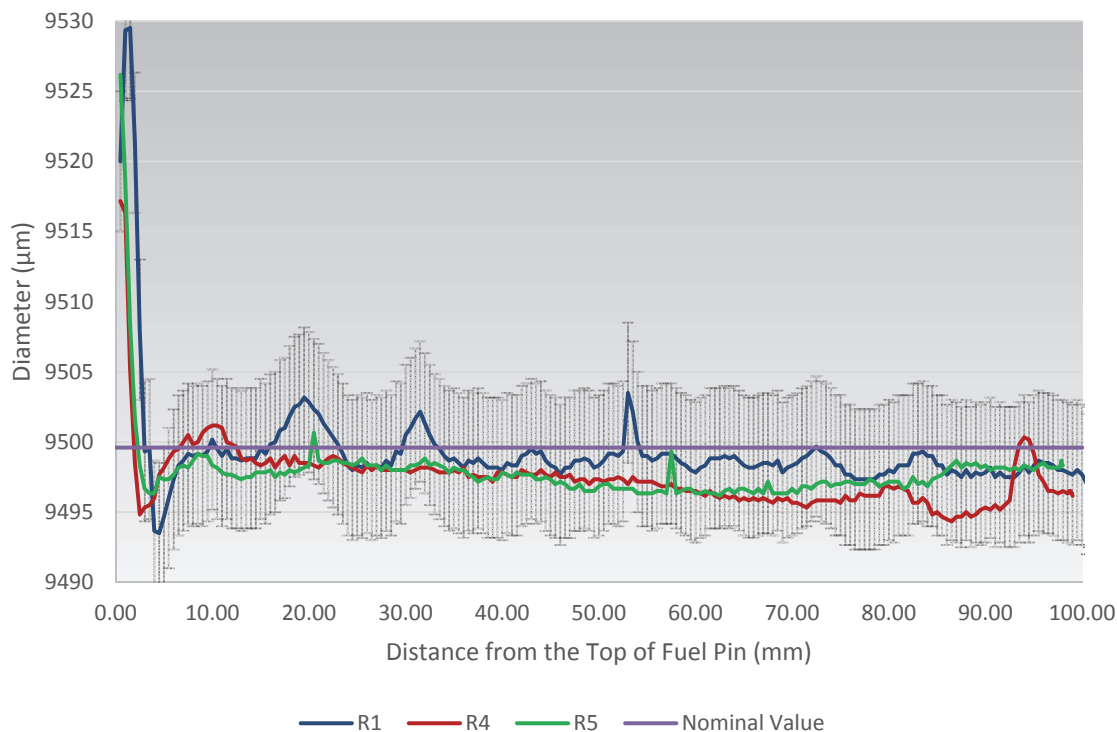


Figure 7. Measurement of fuel rod diameter along the rodlet axial length for the three rods. For each axial location, error bars represent 95% confidence interval of the mean value calculated over seven different orientations. The purple line represents the nominal as-fabricated diameter value.

3.1.3 Gamma Spectrometry

Gamma ray spectrometry of all of the ATF-1A rodlets was performed using the HFEF Precision Gamma Scanner (PGS). The PGS has three major components: collimator, stage, and detector. The collimator penetrates the HFEF cell wall with a rectangular aperture that is adjustable from 0.254 cm to 0.00254 cm in height and is 2.2225 cm wide. The collimator can be rotated from a horizontal to vertical orientation. The stage manipulates the sample in front of the collimator in the plane facing the collimator and can rotate the sample about its central axis. The detector consists of a Compton suppressed high purity germanium detector, and its control system moves the stage and collimator and initiates the scans.

Axial gamma spectrometry of all the rodlets showed that most detectable fission products (^{144}Ce , ^{95}Zr , ^{154}Eu , ^{106}Ru , among others) were well incorporated into the UO_2 major phase. Some discrepancies were observed in the ^{134}Cs and ^{137}Cs signals. Rodlets R1 and R4 show an almost constant profile for Cs isotopes along the enriched fuel stack, with signal depression occurring at the pellet-pellet interfaces, as typically observed in pellet bearing LWR pins. No extensive axial redistribution of cesium was observed (Figure 8a and Figure 8b). For these two rodlets, the observed ^{134}Cs to ^{137}Cs activity ratio was used to calculate the axial burnup profile of the rodlets, where the burnup was scaled from the value obtained from analytical chemistry measurements in Table 1.

The gamma scanning profile of the UO_2 -diamond rodlet (R5) is less prototypical and shows a more irregular axial profile (Figure 8c). The pellet-pellet interface location cannot clearly be identified from the ^{137}Cs activity signal, and partial migration of ^{137}Cs occurred, resulting in signal local spikes. It is to be noted that the destructive examinations revealed extensive microcracking of the entire fuel pellets, as discussed below in further detail. Most likely, the extensive cracking of the fuel matrix has favored release of cesium, resulting in the irregular axial profile observed. The microstructure cracking could also

explain the enhanced fission gas release. The axial burnup profile was not calculated for this rodlet due to the partial cesium redistribution.

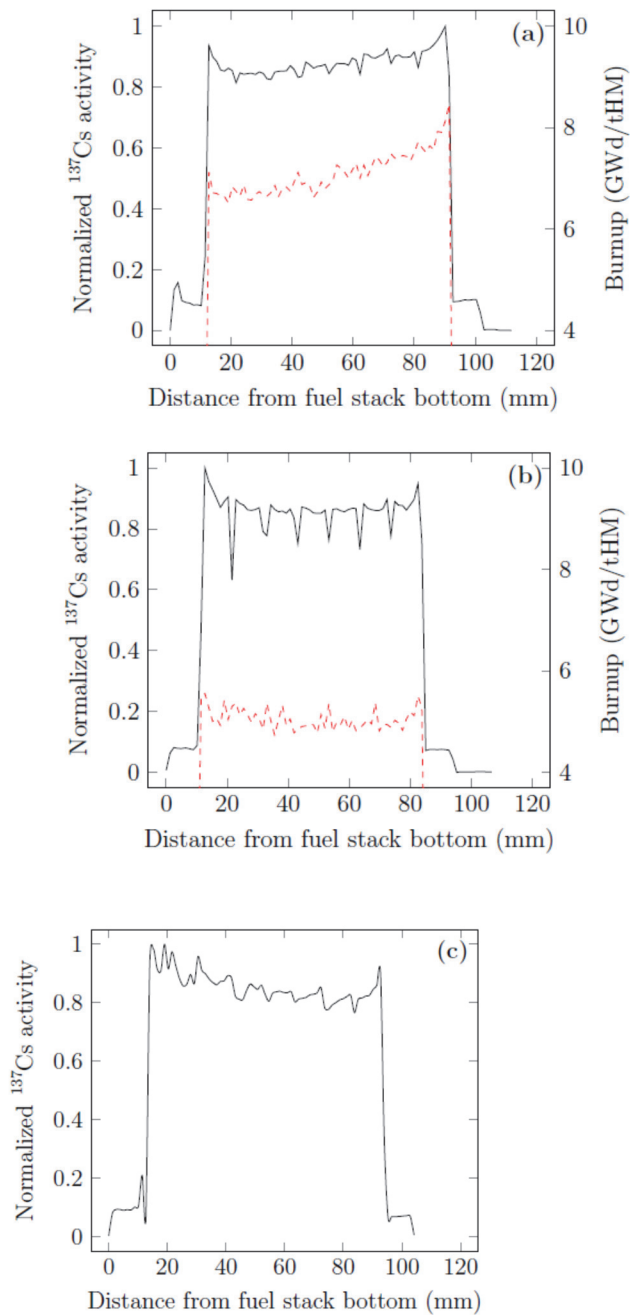


Figure 8. Axial gamma scanning of ^{137}Cs for (a) R1, (b) R4 and (c) R5 (black, solid lines). In (a)-(b) the calculated axial burnup profile is also shown (dashed line).

3.1.4 Fission Gas Release

Fission gases were collected from the rodlets using the HFEF GASR system. Rodlets were punctured using a 150 W Nd-YAG laser system, and a gas sample was collected in a stainless steel bottle external to

the hot cell. Void volume in the rodlet was then determined by a series of backfills into the punctured rodlet and expansions into the GASR system. The rodlet internal gas pressure was derived from the void volume measurement and the initial gas pressure measurement upon puncture. Fission gas analysis was performed by gas mass spectrometry. Results of fission gas analysis provided total elemental composition, krypton isotopic composition, and xenon isotopic composition.

Table 2 summarizes the calculated fuel centerline irradiation temperature range, measured burnup and fission gas release of the three rodlets. The absolute value of fission gas release for the rodlets R1 and R4 falls in the expected range per calculation by the Vitanza curve [34]. Instead, fission gas release for the R5 pin exceeds the value expected by the Vitanza curve. This result is discussed further below in the context of the observed microstructure of this fuel.

Table 2: Irradiation data for the ATF-1A rodlets

Rod ID	Fuel	Fuel centerline temperature range (°C)	Burnup (GWd/tHM)	Fission Gas Release (%)
R1	UO ₂	1250-1500	7.2	2.24
R4	UO ₂ -SiC	1500-1800 ^a	4.9	0.63
R5	UO ₂ -diamond	1000-1200 ^a	7.2	1.08

^aThe temperatures were calculated using the values of thermal conductivity provided in Refs. [9] and [12], respectively.

3.1.5 Burnup

During rodlet sectioning to create the microscopy samples, additional samples were taken from near the fuel column mid-plane and sent to the INL Analytical Laboratory (AL) for a variety of chemical and isotopic analyses. The primary goal of these analyses was to ascertain the burnup of the sampled material. Gamma spectrometry analysis was also performed.

Burnup is calculated from the results of mass spectrometry measurements of dissolved fuel samples. The fuel is dissolved and aliquots are sent through several different inductively coupled plasma, mass spectrometry (ICP-MS) devices. A chemical separation for Pu was performed to help fully analyze the actinide content of the fuel. The determination of burnup was performed using the measured mass of a specific fission product in the fuel, the cumulative fission yield of that specific fission product, and the total mass of actinides present in the sample. This method is sometimes referred to as the “Fission Product Monitor - Residual Heavy Atom” technique [31,33] and calculates burnup in Fission per Initial heavy Metal Atoms (%FIMA). All fission yields were taken from ENDF/B-VII.1 [35]. A benefit of this burnup technique is that it requires no *a priori* knowledge of the sample.

The measured burnup values are shown in Table 2. The burnup was calculated using the measured actinide concentration and the concentration of the following nuclides: La-139, Ce-140, Ce-142, Pr-141, Nd-145, and Nd-146. The burnup values match the prediction fairly well.

3.1.6 Optical Microscopy

Microscopy samples for investigation of the microstructure were prepared using standard metallographic techniques and examined by a Leica DMI8 microscope installed in the hot cell. Two microscopy samples were prepared from each rodlet, one transverse cross section and one longitudinal cross section. The transverse section was taken from the top half of the fourth enriched fuel pellet, starting from the top of the fuel column, while the longitudinal section was prepared from the third enriched pellet. The fuel pellet from the UO₂-SiC rodlet selected for the longitudinal microscopy sample was too fractured to maintain its geometry, and this sample was not further analyzed. Results from optical microscopy of the pins are shown in Figure 9 to Figure 10. These figures contain highlights from both the transverse and, when available, longitudinal mounts prepared for examination.

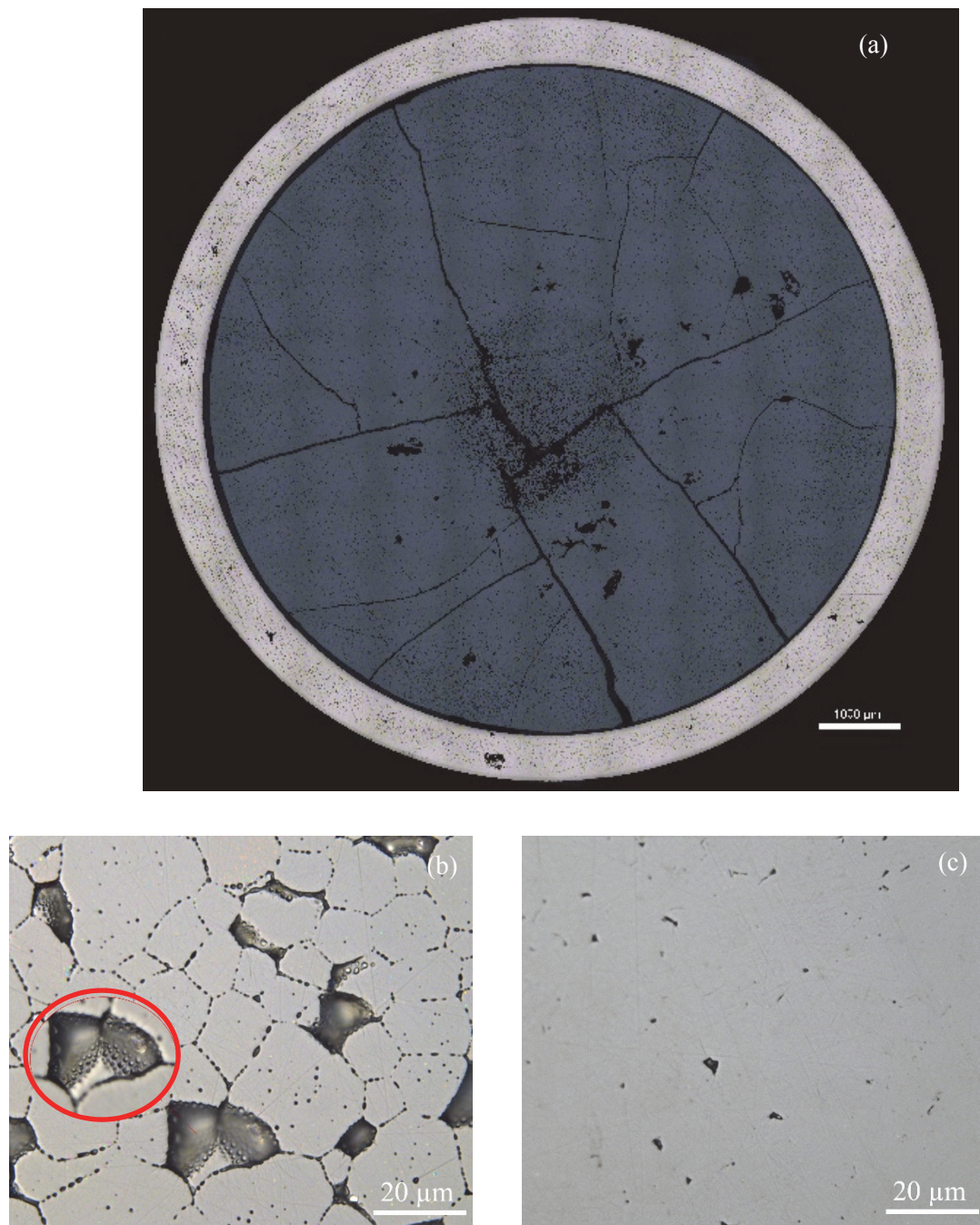


Figure 9. (a) Low magnification ceramography cross section of R1. (b) High magnification image of the inner part of the pellet ($r/r_0 < 0.3$). Red circle highlights the grain boundary covered by fission gas bubbles. (c) High magnification image of the external part of the pellet ($r/r_0 > 0.3$).

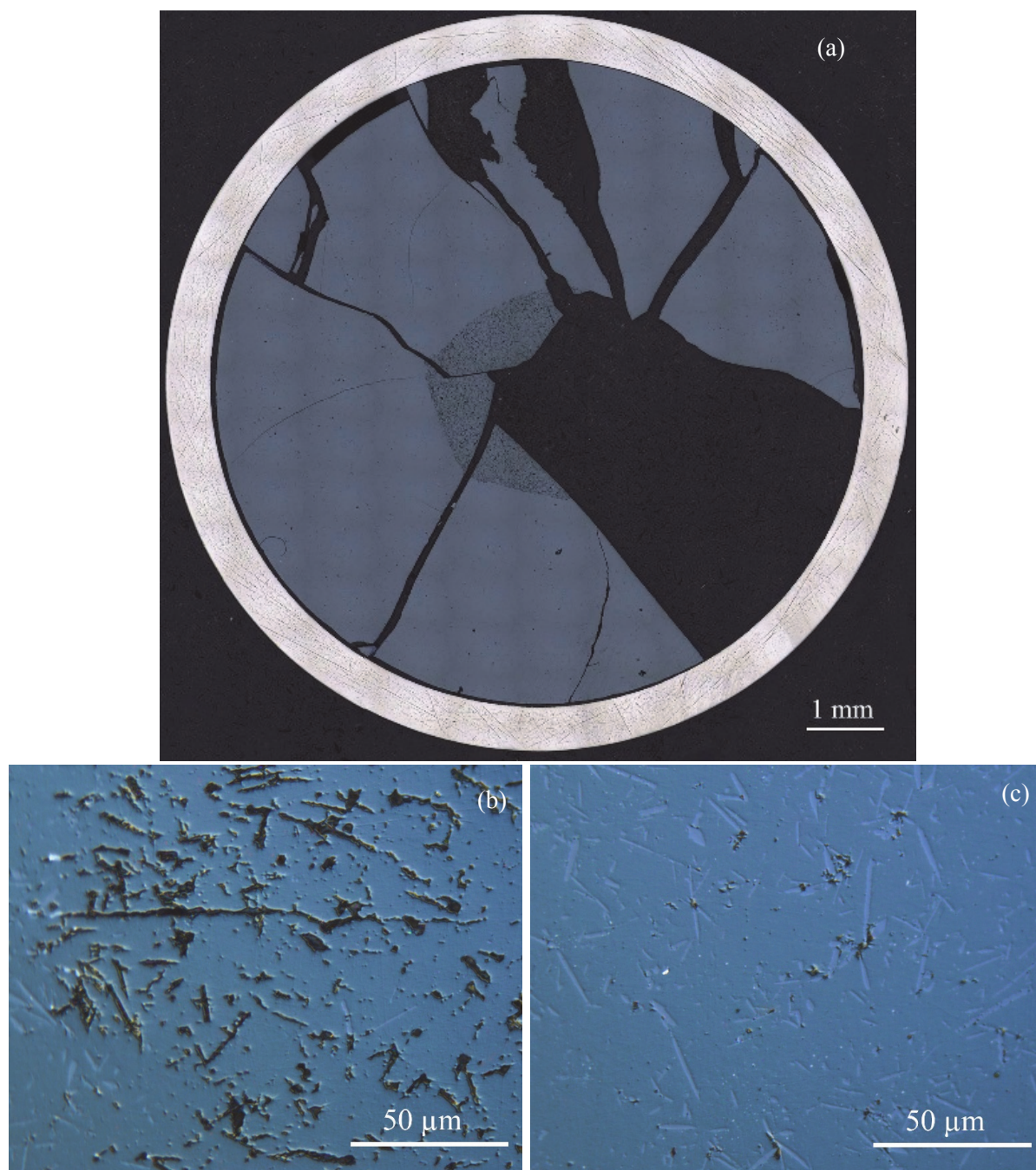


Figure 10. (a) Low magnification ceramography cross section of R4. (b) High magnification image of the inner part of the pellet ($r/r_0 < 0.32$). (c) High magnification image of the external part of the pellet ($r/r_0 > 0.32$)

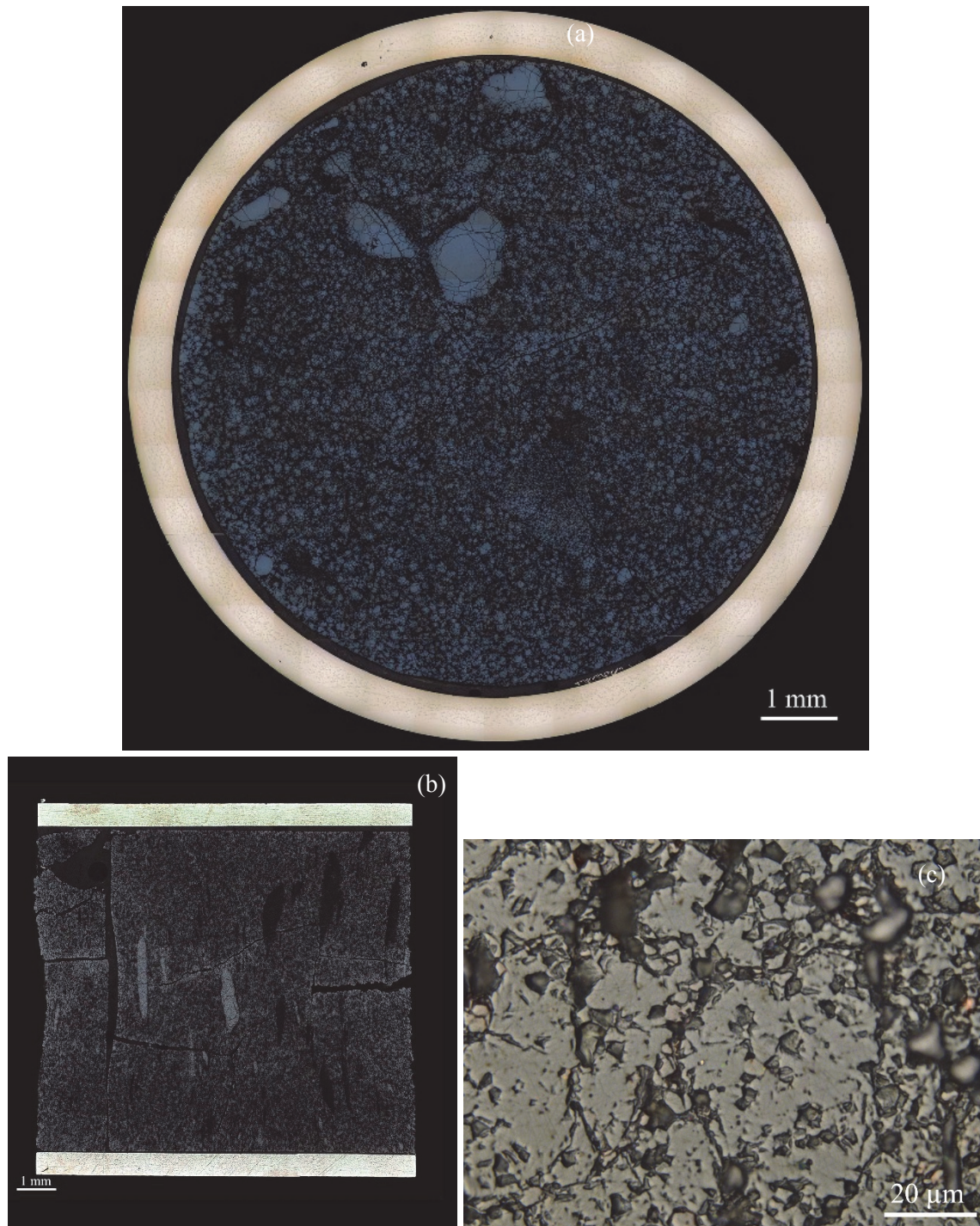


Figure 11. Low magnification (50x) ceramography samples of R5 showing a (a) radial cross section and a (b) longitudinal section. (c) High magnification image (1000x) highlighting the cracked pellet matrix

3.2 Discussion

Neutron radiography data on all the rodlets showed relatively good fuel performance without any gross fuel relocation (Figure 5). From the neutron radiography, the UO_2 -SiC rodlet appears more fractured compared to the UO_2 rodlet, as confirmed by visual inspection of the rod once cut (Figure 10a). No extensive macroscopic cracking is visible in the UO_2 -diamond rodlet, but from the optical microscopy images, it is apparent that the fuel microstructure has been severely disrupted during irradiation, revealing micro-cracking along the entire pellet (Figure 11). The fine cracking could not be captured by the neutron radiography, as the crack size is below the spatial resolution limit achievable by the current neutron imaging capabilities.

Regarding the UO_2 sample, low magnification macrograph reveals a central region with different texture compared to the rest of the fuel pellet. This is related to fission gas bubbles switching position from dissolved and intragranular to intergranular. From application of image analysis techniques (details below), the radial extent of such zone was determined to be 30% of the pellet radius or $r/r_0=0.3$ where r_0 is the outer radius of the pellet. Outside this region, image analysis was carried out to quantify porosity. The porosity radial profile is shown in Figure 13. The profile changes along the fuel radius, but the overall average value remains close to the as-fabricated porosity. High magnification images highlighted that the different appearance of the matrix texture in the central region is related to extensive grain pull-out and intergranular precipitation of large fission gas bubbles, which are partially interconnected along the grain boundaries (see Figure 9b). Such extensive bubble precipitation and interconnection is atypical for UO_2 pellets at such low burnup, but it can be explained by noting that the temperatures experienced by the fuel in this region exceeded 1200 °C (Figure 12a) throughout the entire irradiation period. Those temperatures are above the normal operating temperatures encountered by the fuel in LWR. Irradiation at such high temperatures, even for short periods of time, causes extensive grain-face swelling, as was observed for instance in Reference [36].

Optical microscopy images of the UO_2 -SiC fuel are shown in Figure 10. In the central region of the pellet, the SiC whiskers appear to have dissolved or have reacted with the matrix (Figure 10b). The relative radial extension of the zone is 32% of the pellet radius as determined from image analysis of the pellet (see below). According to fuel performance calculations, the local temperatures at relative radii <0.32 were in the range 1300 °C to 1800 °C. In this temperature range and considering the likely variation of the oxygen-to-metal ratio occurring during irradiation, thermodynamic calculations predict formation of several compounds and phases, including liquids [37]. From optical microscopy images only it is not possible to determine which of those phases or compounds might have formed changing the microstructure appearance. Further advanced analysis like Scanning Electron Microscope (SEM) and Energy-dispersive X-ray Spectroscopy are necessary to fully elucidate the status of the fuel microstructure in this zone. Such analyses go beyond the scope of the present baseline PIE, which are aimed at determining exclusively the principal fuel performance parameter of merits, i.e., fission gas release, fuel microstructure integrity, eventual presence of fuel-cladding interaction, and cladding strain.

Representative samples cut from rodlet R5 are shown in Figure 11. As already mentioned, the diamond-doped pellets were severely damaged during irradiation. As a result of matrix fragility, severe pull-out occurred during the preparation of the ceramography samples, as highlighted in the high magnification image shown in Figure 11c. Multiple factors could have contributed to the microstructural instability. On one side, diamond has a thermal expansion coefficient approximately half of the UO_2 one in the temperature range experienced by the rodlet. Such difference induces residual thermal stresses during power excursions which would induce micro-cracking at the inclusion interface [38]. On the other side, calculated phase diagrams for the system U-O-C in the temperature range 600 °C to 1100 °C show that graphitization and formation of either U_2C_3 or gas is to be expected in the fuel matrix, depending on the stoichiometric shift [39,40]. Fission gas release measurements showed an increased amount of CO_2 in the released gas mixture from this rodlet compared to the amount released by the UO_2 pin, corroborating the hypothesis of diamond graphitization. Graphitization of the diamond particles would result in degraded thermal and mechanical properties of the composite, raising temperatures, and possibly initiating a

positive feedback on the structural instability of the fuel. On the basis of the present postirradiation examinations, it is not possible to establish the final cause leading to such structure instability. X-ray micro-diffraction and more advanced microstructural analysis (e.g., SEM) are required to determine the reasons of the damage and if uranium carbides or other compounds have formed.

Image Analysis

The microstructure of pellets belonging to rodlets R1 and R4 has been segmented using both region- and texture-based segmentation methods. The low magnification (50x) macrographs were initially segmented into four relevant regions using a k-means segmentation algorithm [41]: background, cladding and fuel pellet, composed of matrix and secondary phases (either porosity or SiC). Subsequently, a local contrast enhancement method is applied to the fuel pellet by calculating the standard deviation in a 5x5 neighborhood around each pixel, in order to highlight the different textures present in the fuel pellet. The central part was then extracted by binarizing the filtered image using the Otsu's thresholding algorithm [42] in order to create the initial mask of the central zone. The mask was then refined using adaptive contour based on the Chan-Vese model [43]. All the algorithms have been implemented in Matlab®. Results for the rods R1 and R4 are presented in Figure 14.

Further analysis was performed on the UO₂ sample to quantify the porosity along the fuel radius. Images at magnification 200x were used in this case. Digital resolution of the images is 4.125 pixel/μm, resulting in a minimum detectable object size of 0.25 μm², according to the Shannon's sampling theorem [44]. The porosity segmentation was achieved by image binarization. Optimal threshold was determined by the Otsu's method. The determined value of the porosity will be influenced by the selected gray-level threshold. An estimation of the error associated to the thresholding process was determined by assuming a variation of 10% from the optimal threshold value. Cracks and potential pull-outs were eliminated on the basis of shape and size. Objects largely exceeding the mean object size and/or extremely elongated were eliminated from the counting and their area subtracted from the total image area.

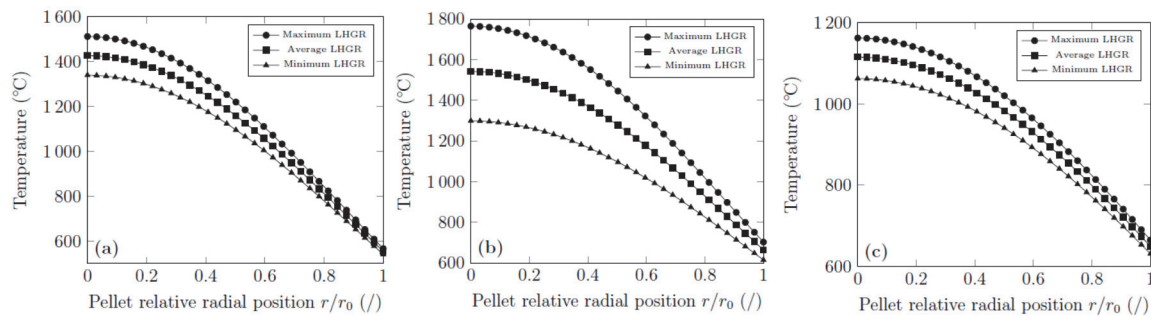


Figure 12: Radial profile temperatures for (a) R1, (b) R4 and (c) R5. Circles: maximum Linear Heat Generation Rate (LHGR). Squares: average LHGR, Triangles: minimum LHGR.

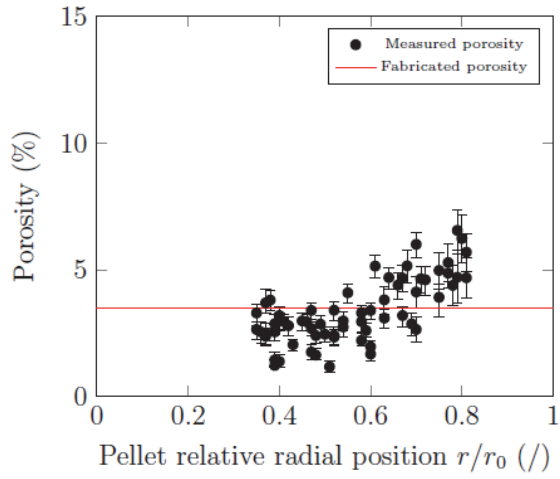


Figure 13: Porosity radial profile for rod R1 (black dots). Average as-fabricated porosity value (red solid line).

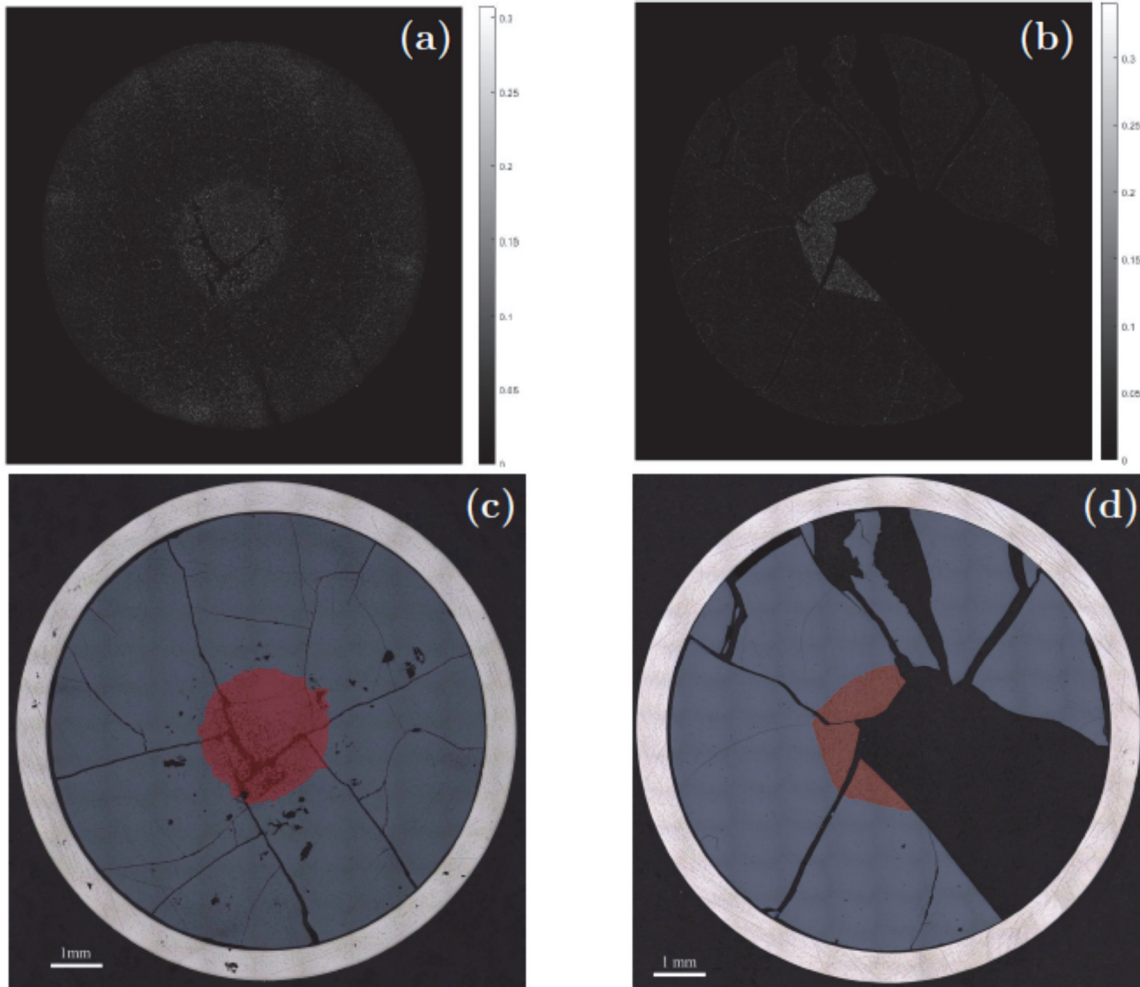


Figure 14. (a)-(b) Result of the application of the standard deviation filter to the low magnification images of R1 and R4, respectively. Resulting final segmentation of the pellet central region based on the algorithm. (c) R1, (d) R4

4. ATF-1W

As with ATF-1A, PIE examinations were performed at the Hot Fuel Examination Facility of INL. Neutron radiography, gamma spectrometry and tomography, dimensional inspection, fission gas release, burnup analysis, optical microscopy, and microhardness testing were carried out. The results of these exams are summarized in the following sections. Advanced image analysis has been performed in order to assess in a more quantitative way possible variation of the microstructure due to the irradiation (see Section 4.2).

Image processing algorithms have also been designed and implemented to analyze the as-fabricated microstructure and the irradiated one. The aim was to perform image segmentation in order to separate and quantify (a) the amount of the secondary phases, (b) the porosity associated with the UO_2 phase, (c) the fission gas bubbles (in the irradiated samples). A simple thresholding of the image is not sufficient to perform the analysis. A binarization of the image is not able to distinguish between the UO_2 phases and the associated porosity, since the two phases are characterized by similar gray-level values. In addition, the majority of the fission bubbles present in the irradiated microstructure are not distinguished from the background. To overcome this issue, a high level vision approach has been used. Specific image analysis segmentation algorithms have been developed by using Matlab®. Two sets of images were available for quantification of the as-fabricated microstructure. For the first set, both Back Scattered Electron (BSE), Secondary Electron (SE), and Energy-dispersive X-ray Spectroscopy (EDX) data were available. The image analysis procedure used to segment the different phases for the first set is detailed in [26]. In the other case, only BSE data were available. In this case, no iron phase could be distinguished from the UO_2 precipitates and porosity, as no topographic information from SE images could be collected. However, due to the limited amount of iron present, the error induced in the areal fraction measurement of the UO_2 and porosity phases remain limited, in particular considering the typical intrinsic errors occurring in phase quantification using image analysis methods, which can be as high as of 2-3% [45]. The algorithm employed for analysis of this second set of images is described in Section 4.2. The phase quantification results are summarized in Table 3. There is good agreement between the estimation in the two set of images, indicating consistency between the outputs of the two segmentation algorithms. The higher values of UO_2 and porosity measured in the second case are likely due to the discrepancy in the iron phase measurement. The data for the as-fabricated pellets support the evaluation of potential changes in the microstructure following irradiation, as explained in Section 4.2.

Table 3: Quantitative image analysis results for the as-fabricated U_3Si_2 microstructure

Image set	Si-rich phase (%)	UO_2 (%)	Fe (%)	Porosity (%)	U_3Si_2 (%)
1	13.1±1.1 ^a	7.0±0.9	0.3±0.3	0.4±0.3	79.2±1.6
2	14.3±3.0	7.5±1.0	n.a. ^b	0.6±0.5	77.6±3.4

^a95% confidence interval

^bNot available

4.1 Results from PIE

Similar to the ATF-1A PIE, ATF-1W PIE began when the capsules entered the HFEF hot-cell. Prior to removing the rodlets from the capsules, visual exams, neutron radiography, and axially resolved gamma spectrometry are performed on the intact rodlets. In ATF-1W, there were no indications of any severe issues with the fuel performance. The rodlets were removed from the capsules and PIE on the rodlets began. Visual inspection was performed on the rodlets and no usual features were detected.

4.1.1 Neutron Radiography

Neutron radiography of the ATF-1W rodlets was performed in a similar manner to ATF-1A. However, the use of the radiography fixture was modified slightly to improve the sharpness of the radiographs.

Radiographs were taken at 6 different angles 30° apart. The capsule neutron radiography is shown in Figure 15, and example rodlet radiographs are shown in Figure 16. No axial growth was detected in the neutron radiography to the limit of resolution in the radiography. The lack of axial growth is significant because the swelling behavior of pellet geometry U_3Si_2 was not well known prior to this test, and there was some concern that this fuel would experience significant swelling even at these low burnups. The fuel appears to have largely maintained its pre-irradiation geometry without significant fuel relocation. There are some cracks present in the fuel from the irradiation, but the number of cracks compared to UO_2 appears small. This was confirmed in optical microscopy (Section 4.1.6).

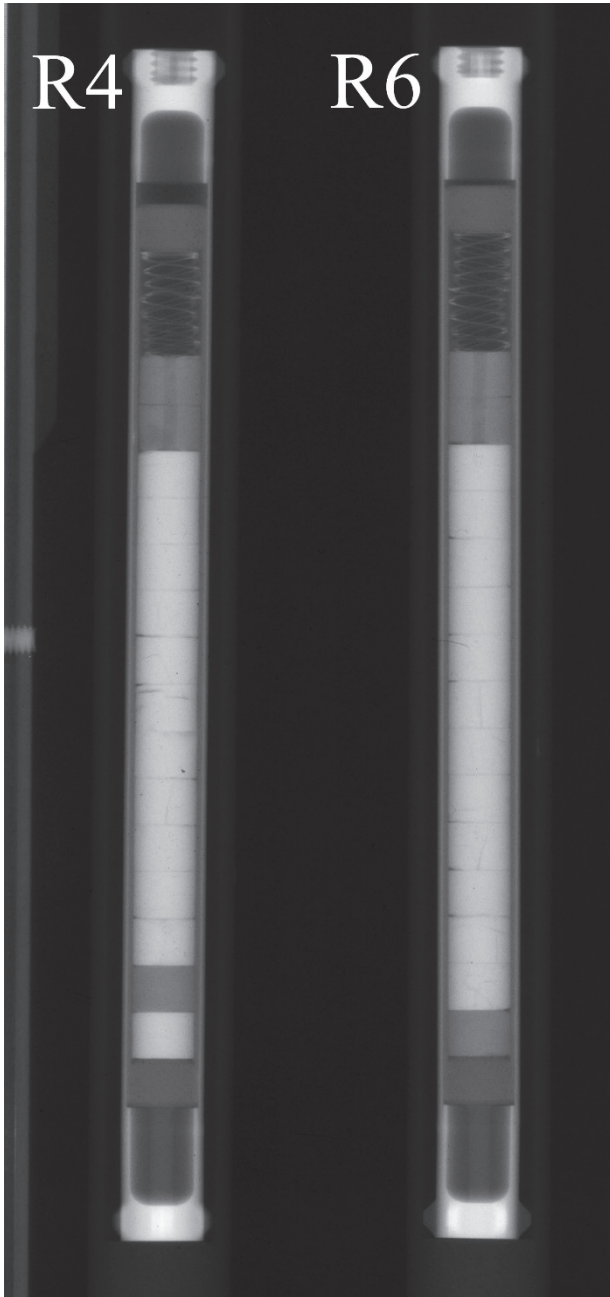


Figure 15. Capsule neutron radiographs of the ATF-1W R4 and R6

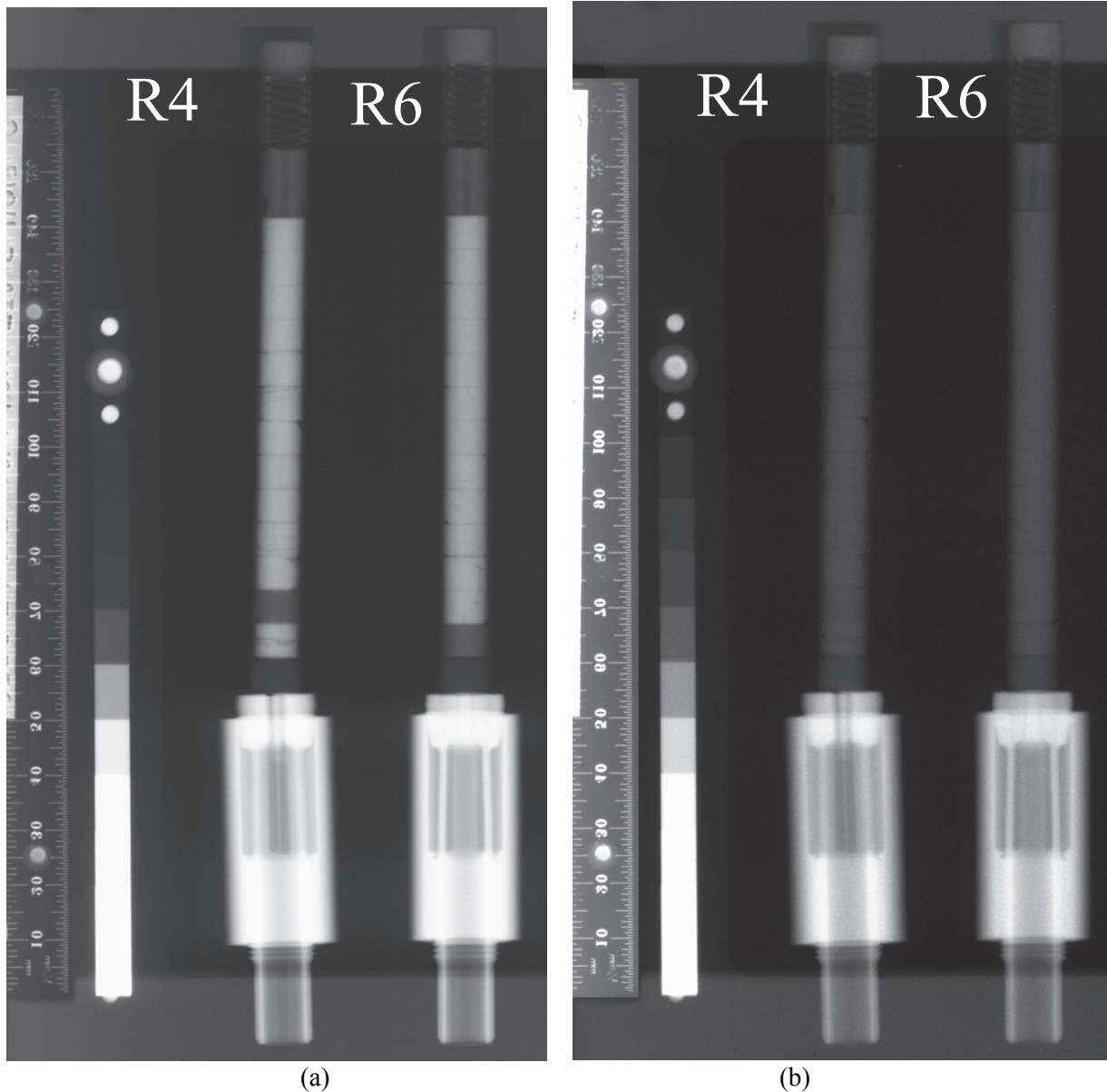


Figure 16. Rodlet neutron radiography of ATF-1W rodlets (a) thermal (b) epithermal

4.1.2 Dimensional Inspection

Dimensional inspection of the ATF-1W rodlets was performed using the US HPRR Plate checker in HFEF. Outside diameter measurements were collected all along the rodlets in roughly 0.5 mm increments and at 36 angles every 5° from the initial scan angle to 180°. Diameter measurements are collected with $\pm 5 \mu\text{m}$ accuracy. The angle averaged measured diameters for the ATF-1W rodlets is shown in Figure 17 for 1W R4 and Figure 19 for 1W R6. The specified cladding dimension is also shown. Because of damage to the endcap during disassembly the R4 was only scanned over the 50 mm that contained the majority of the fuel (see Figure 18). The bump in Figure 17 near 45mm is the endcap weld for this pin. The scan of ATF-1W R6 is reversed with the bottom end cap at the left side of the plot, and the spike at 5mm is the weld on the bottom endcap. No significant radial strain of the cladding resulting in excessive diametral change of the pins was detected during dimensional analysis. The diameter value, when including the experimental uncertainty, is close to the nominal one along the entire rod axial length in both cases.

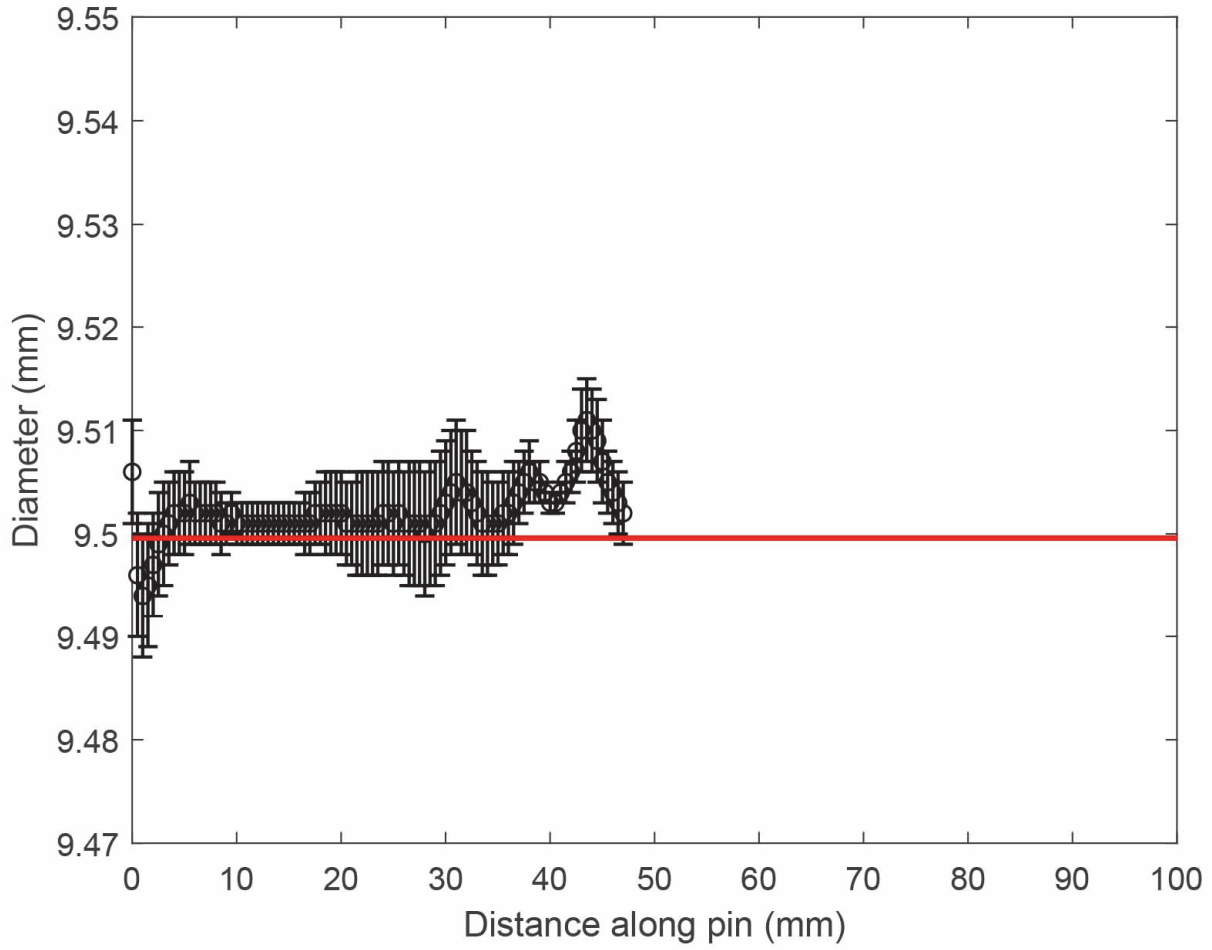


Figure 17. Dimensional measurements of ATF-1W R4. The measured value represent the average of measurements taken every 5°. Red solid lines indicate the nominal values.



Figure 18. Dimensional inspection of ATF-1W R4 showing the probes at the 0 Position of Figure 17

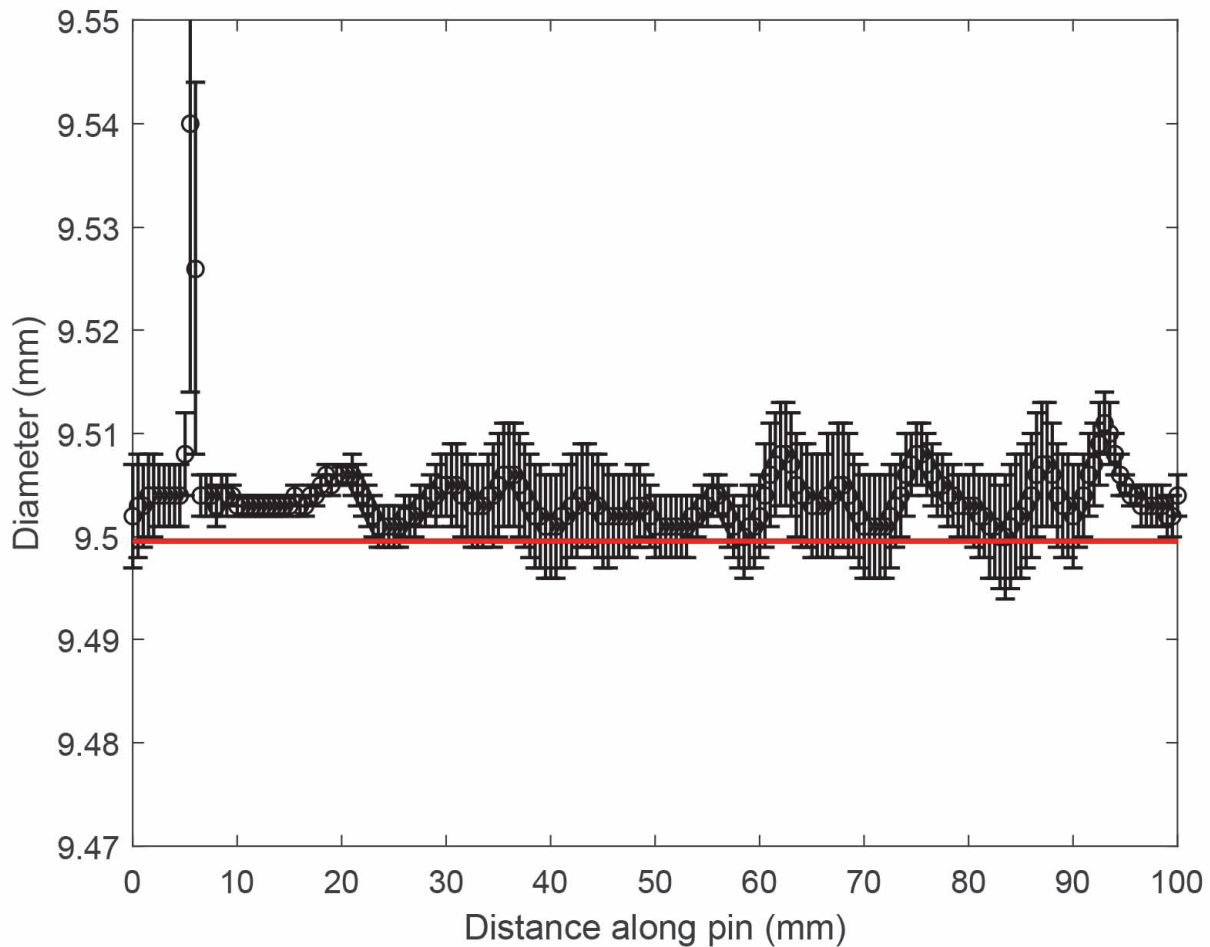


Figure 19. Dimensional measurements of R6. The measured value represent the average of measurements taken every 5°. Red solid lines indicate the nominal values.

4.1.3 Gamma Spectrometry

Gamma ray spectrometry of the two rodlets was performed with the HFEF PGS. The axial scan of ATF-1W R6 is shown in Figure 20 for select radionuclides. The graph contains 3 different radionuclides that represent 3 different classes of fission products (Cs, noble metals, and lanthanides). All these radionuclides appear to be well incorporated into the fuel matrix with no detectable axial migration of fission products.

In addition to axial gamma spectrometry scans, it is possible to rotate the HFEF PGS collimator from a horizontal to a vertical orientation. In this orientation, it is possible to move an axial level of the fuel past the collimator and perform a series of rotations over several angles. The resulting signals over several angles can be collected and tomographically reconstructed to provide a two dimensional distribution of fission products averaged over an axial location. This is referred to as Gamma Emission Computed Tomography (GECT). The full details of this technique are available in Reference [46], and the demonstration of this technique can be seen in Reference [47] and [48]. This technique is similar to conventional X-ray computed tomography, but it is limited by the number of angles that can practically

be collected as spectrum collected takes several minutes and the total collection time can extend to several days or weeks for a fully characterized rodlet.

The two-dimensional distributions of Cs-137, Zr-95 and Ce-144 are reported in Figure 21a for ATF-1W R4 and Figure 21b for ATF-1W R6. The areal distribution of all the products remains fairly homogeneous. A minor increase in the fission product concentration along the pellet periphery was expected due to the local increase of burnup following self-shielding, which is typical of a thermal neutron spectrum.

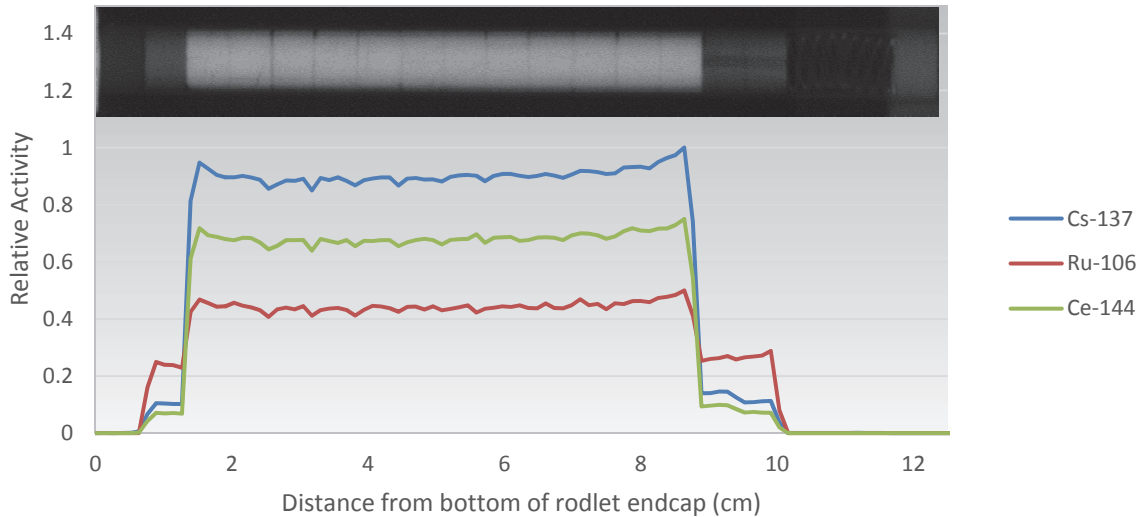


Figure 20. Axial distribution of select gamma emitting radionuclides in ATF-1 W R6

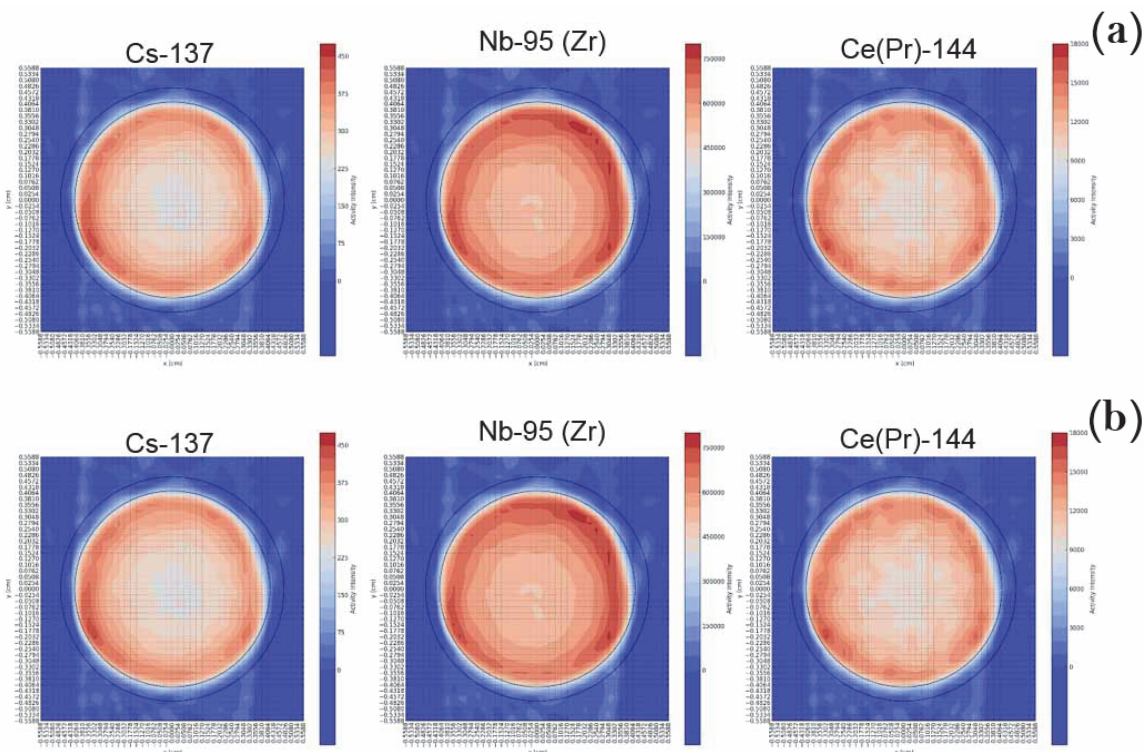


Figure 21. Two-dimensional gamma spectrometry of major radionuclides for (a) R4 and (b) R6.

4.1.4 Fission Gas Release

Fission gases were collected from the rodlets using the HFEF (GASR system in the same manner as ATF-1A). Fission gas analysis was performed by gas mass spectrometry. A summary of the fission gas release results for ATF-1W is shown in Table 4. The first column is the fission gas release based on the predicted number of fissions, and the second column is the fission gas release based on the measured number of fissions based on the mass spectrometry results discussed in Section 4.1.5. Table 4 summarizes the calculated average irradiation temperature and LHGR, measured burnup and Fission Gas Release (FGR) of the two rodlets. Despite the higher irradiation temperature, FGR from R6 remains very low as for R4.

Table 4: Irradiation data for the ATF-1W rodlets.

Rod ID	Average irradiation temperature (°C)	Average linear heat generation rate (W/cm)	Burnup (GWd/tHM)	Fission Density (fissions/cm ³)	Fission Gas Release (%)
R4	900	421	17.1	4.94x10 ²⁰	0.05
R6	1200	441	19.6	5.88x10 ²⁰	0.05

4.1.5 Burnup

During rodlet sectioning to create the microscopy samples, additional samples were taken from near the fuel column mid-plane and sent to the INL Analytical Laboratory (AL) for a variety of chemical and isotopic analyses. The primary goal of these analyses was to ascertain the burnup of the sampled material. Gamma spectrometry analysis was also performed. Burnup and fission density is calculated as discussed in Section 3.1.5.

The measured burnup values, the measured fission densities, the calculated burnup, and calculated fission density for each rodlet are shown in Table 4. The measured and simulation burnup values agree adequately.

4.1.6 Optical Microscopy and Microhardness Testing

Several samples were cut to analyze the effects of irradiation on the microstructure. Examples of cross-sections are given in Figure 22a for 1W R4 and Figure 22b for 1W R6. Figure 23 shows examples of the microstructure evolution along the pellet radius for the two rods. The appearance of the microstructure in the two cases is very similar. Comparing Figure 23 to the as-fabricated microstructure in Figure 1, no striking changes are evident on the basis of a qualitative analysis, at least on the pellets periphery. The large voids visible in Figure 22a and Figure 22b are pull-outs occurring during the sample preparation. As in the as-fabricated microstructure, secondary light and dark phases are present in the main matrix. On the basis of SEM and X-Ray Diffraction (XRD) analyses reported in [25], those are Si-rich and UO_2 minor phases formed during fabrication. Porosity is co-localized with the UO_2 phases as in the as-fabricated U_3Si_2 . Towards the pellet center, additional small spherical features appear (Figure 23a to Figure 23d and Figure 23f), which are likely due to formation of fission gas bubbles. Si-rich phases cannot be quantified from optical microscopy images, as the Z-contrast discrimination offered by the BSE technique is not available. Also the iron precipitates cannot be distinguished from the UO_2 phase and porosity.

In addition to optical microscopy, Vickers microindentation has been performed using a LECO AMH55 microscope equipped with a Micro/Macro Vickers Hardness Testing System. The measurements were performed at room temperature under argon protective atmosphere. A 500 gf load was applied with dwell time of 13 s, in order to compare the present results with those reported by Harp et al. [25] on the as-fabricated samples. The Vickers hardness number was computed as follows,

$$HV_{0.5} = 0.0018544 \frac{P}{d^2} \quad (1)$$

where P (gf) is the applied maximum load and d (μm) is the average length of the two diagonals of the indentation prints. The hardness value was calculated from the average of five indentation at each radial position [49].

Figure 24 shows the radial profile of the measured Vickers number for both rods. Also the average Vickers hardness number for the unirradiated U_3Si_2 is reported [25]. No significant differences in the local microhardness are measured between the two rods. Minor hardening after irradiation occurs (Figure 24). This can be expected due to accumulation of irradiation-induced defects and chemical hardening following generation of fission products [50]. Figure 25 shows examples of the indentation prints using bright field microscopy in Figure 25a and Figure 25c, and differential interference contrast (DIC) microscopy in Figure 25b and Figure 25d. This second configuration emphasizes edges and surface topography. Some of the imprints show nucleation of radial cracks (Figure 25a). Those can either be formed during loading if the critical load is exceeded, or during the removal of the indenter at loads less than the critical load. In few cases, further growth of the radial cracks was observed, as documented in Figure 25c. No lateral vent cracks were seen in any of the indents. Occasionally, spallation of the imprint edges occurred (see Figure 26). Those indentations were not used in the calculation of the hardness number, as suggested by the ASTM standard [49]. It can be noted in Figure 24 that the hardness value at intermediate radial positions of rod R4 is affected by large scatter. Inspection of the imprints (for example see Figure 27) did not show extended cracking or local failure of the sample surface under the indenter. Series of slip lines parallel to the indent edges were observed (arrows in Figure 27), suggesting a local increase in the capabilities of deformation to satisfy the strain fields imposed by the indenter. The reason for this local behavior is presently unknown. If the area underneath the imprints could be exposed by

Focused Ion Beam (FIB) milling, microstructure morphology investigation using Scanning Electron Microscope (SEM) or TEM could clarify the reasons of the observed behavior.

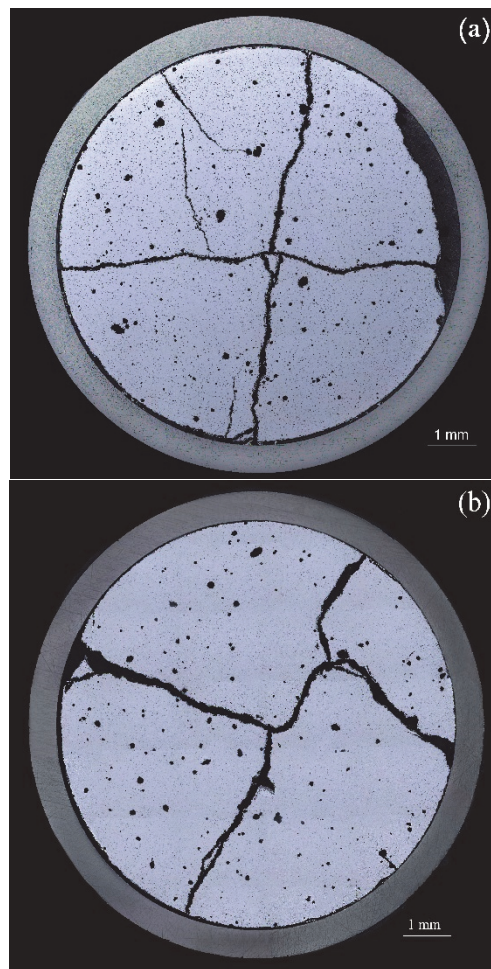


Figure 22. Low magnification (50x) ceramography cross section of (a) R4 and (b) R6.

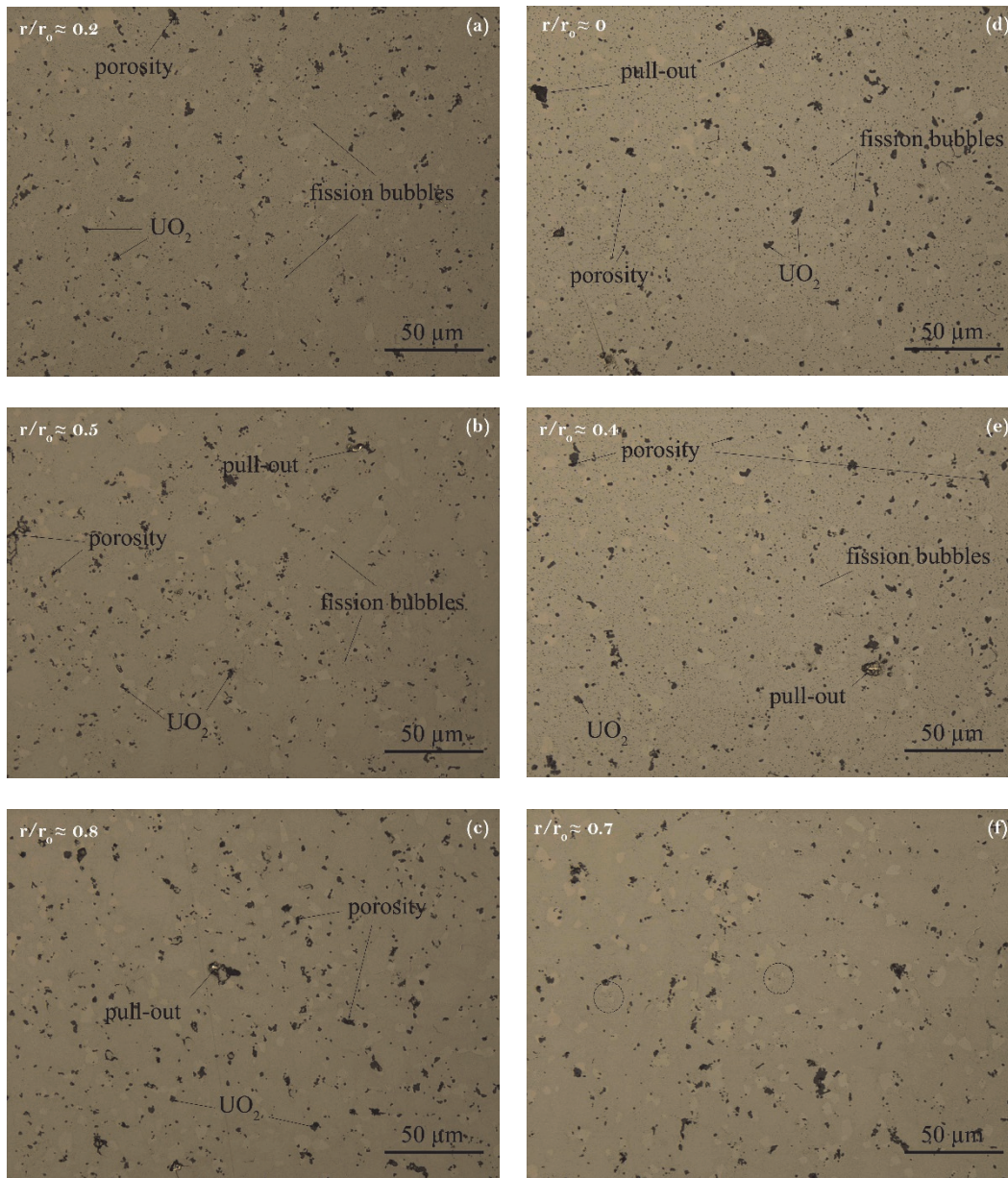


Figure 23. High magnification images of the irradiated microstructure from rodlet (a)-(c) R4 and (d)-(f) R6. The dashed circles in Fig. 12f indicate very tiny fission gas bubbles.

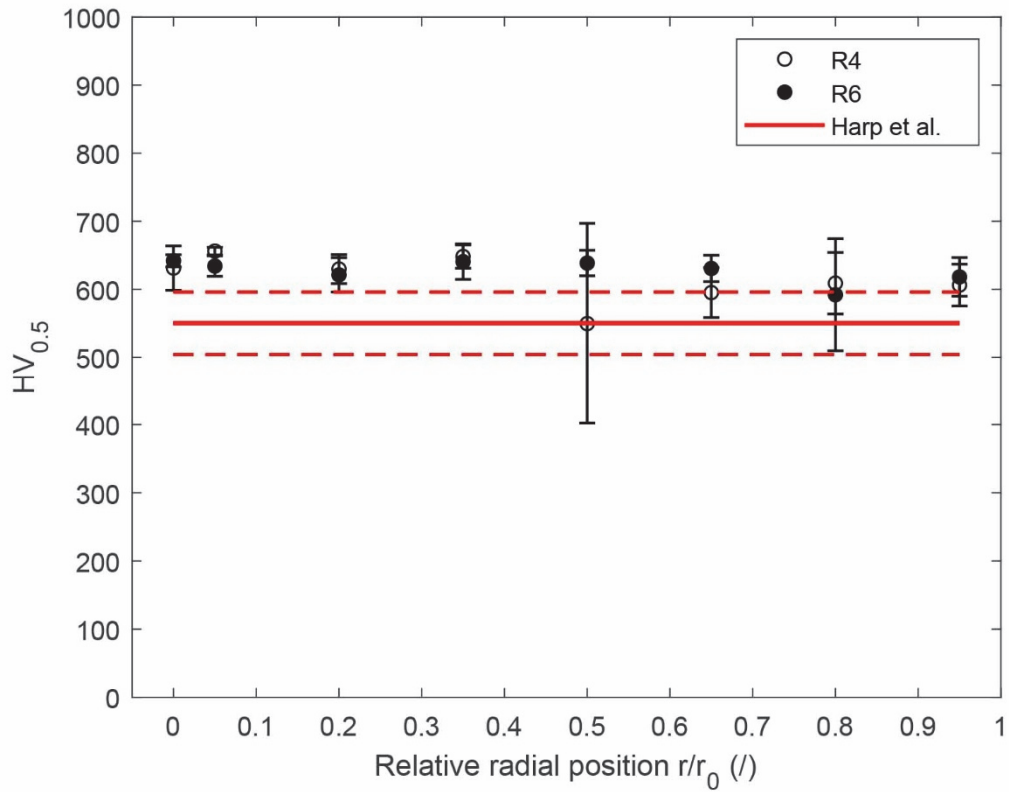


Figure 24. Radial profile of the microhardness for the two irradiated rods. The average microhardness of unirradiated U_3Si_2 [15] is also reported in red.

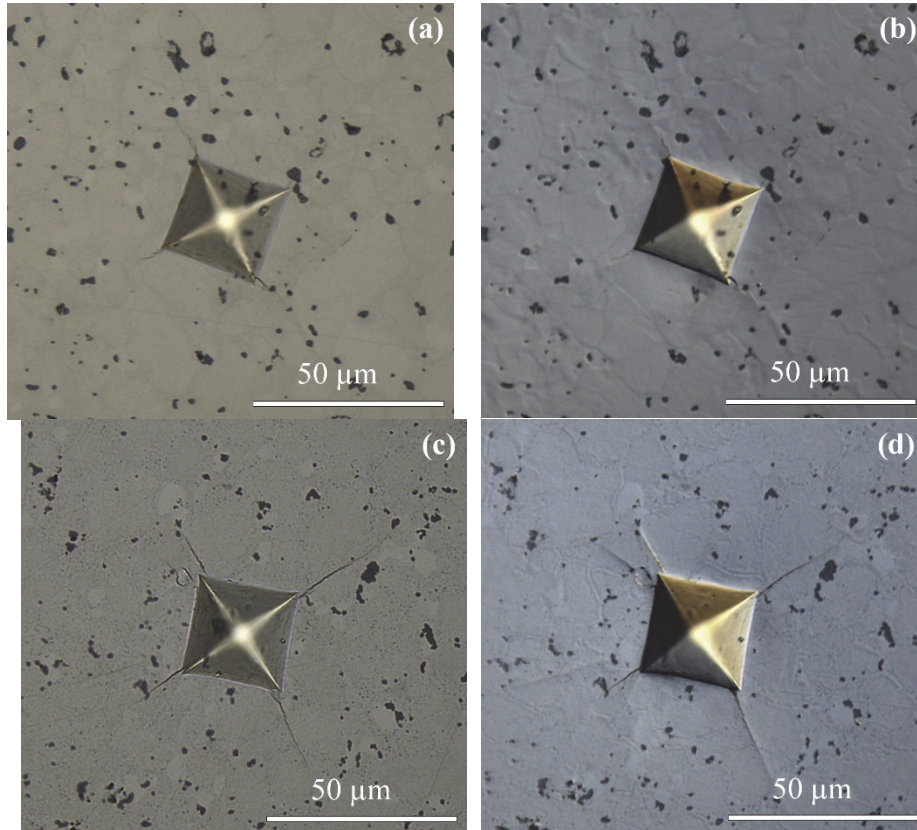


Figure 25. Indentation imprints. (a), (c): bright field microscopy; (b), (d): DIC microscopy. Magnification: 500X.

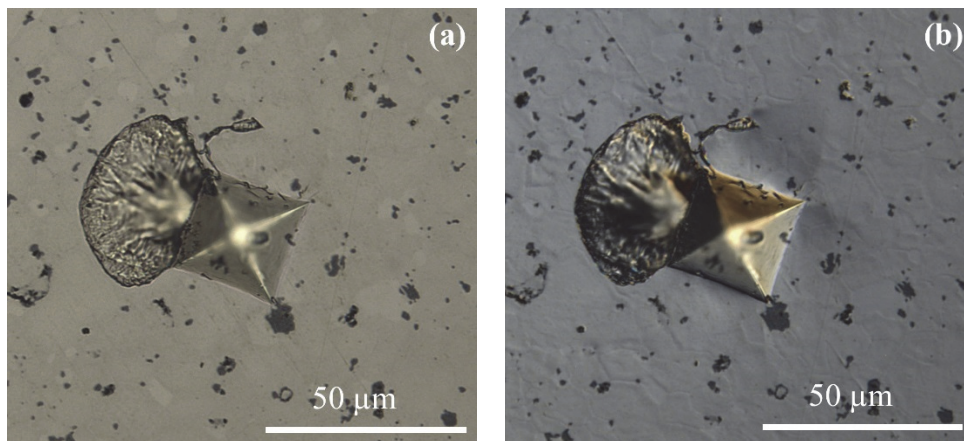


Figure 26. Indentation imprint showing edge spallation. (a): bright field microscopy; (b): DIC microscopy. The use of DIC images highlights partial sink in of the surface next to the indentation. Magnification: 500X

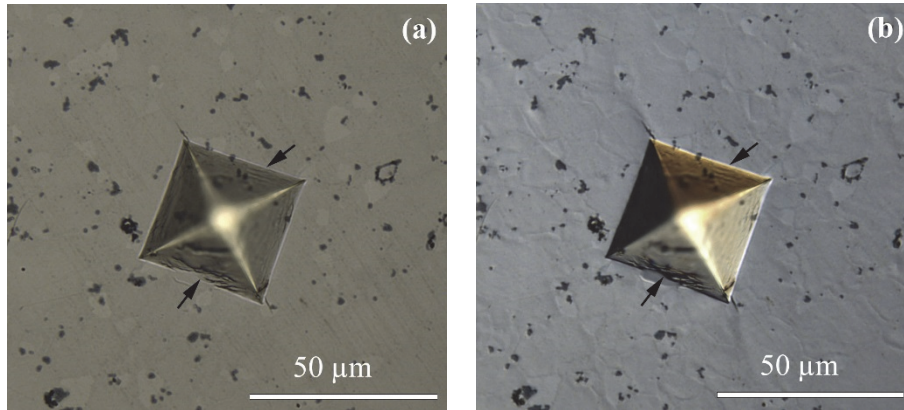


Figure 27. Indentation imprint showing slip lines parallel to the imprint edges. (a): bright field microscopy; (b): DIC microscopy. Magnification: 500X

4.2 Discussion

Overall, the performance of the U_3Si_2 in this irradiation was very favorable. At these irradiation conditions, there do not appear to be any issues with swelling, fission gas release, amorphisation, or fuel cladding interaction. In the neutron radiography, cracks are visible in some of the pellets, but it is not severe. There is only minor diametral strain measured on the cladding (see Figure 18 and Figure 19), confirming the limited swelling of the pellets. The cracking seen in the optical microscopy is a notable difference between UO_2 and U_3Si_2 . As shown in Figure 28, the number of fragments measured from optical microscopy cross sections (see for example Figure 22) lies well below the expected number of fragments for UO_2 pins irradiated at the same LHGR [51]. This is a direct consequence of the reduced thermal stresses in U_3Si_2 that are a result of the higher thermal conductivity of U_3Si_2 . Optical microscopy also reveals that the gap is still open between the pellet and the cladding.

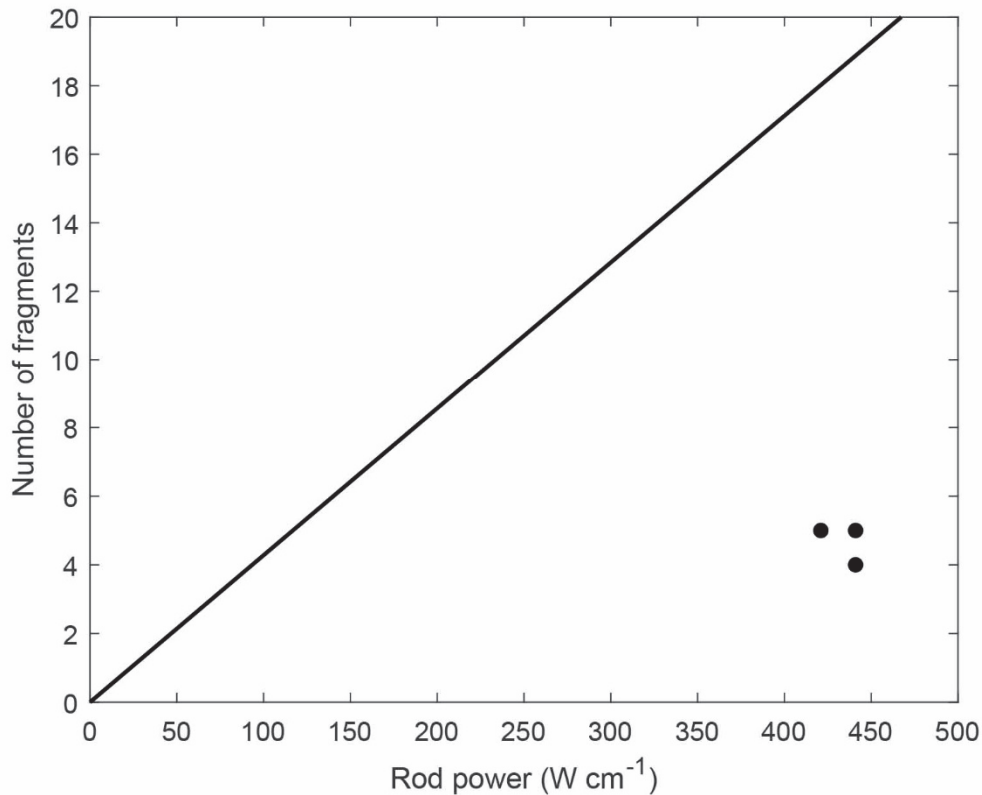


Figure 28: Measured number of pellet fragments from ceramography cross sections of U_3Si_2 fuels (black dots). Expected number of fragments in UO_2 pellets as a function of the average LHGR [51].

The image analysis applied to this fuel allows for a much more quantitative analysis of this fuel and the as-fabricated fuel. The segmentation algorithm used here is limited to the separation of UO_2 , porosity, and fission gas bubbles only (see Section 4.2.2). The main issue in the segmentation of the bubbles is their similarity with the smallest UO_2 precipitates both in terms of grey-level and shape. In addition, their size is close to the resolution limit of optical microscopy, making their discrimination from the image background noise challenging. A definition of “ground truth” (what is precipitate and what is bubble) becomes problematic, resulting in a source of intrinsic uncertainty in the processing of the images and quantification of both UO_2 phase and fission gas bubbles. Since a well-defined automatic discrimination based on absolute values of size, shape or color could not be performed with certainty, a supervised discrimination criterion was introduced at the beginning of the analysis, assuming that the UO_2 precipitates size distribution does not change during irradiation. Figure 29 shows that $\approx 85\%$ of the UO_2 precipitate size is above $0.3 \mu m^2$ in the as-fabricated microstructure. This value is taken as the discrimination threshold. All round features segmented smaller than the pre-determined area are considered fission gas bubbles. The results of the analysis are presented as a function of the rods radial profile in Figure 30 and Figure 31. The average value of the porosity associated with the UO_2 precipitates is in excellent agreement with the average values measured in the as-fabricated microstructure. The average values for the UO_2 precipitates, 4.5% and 5.8% for R4 and R6, respectively, lie below the average values measured in the as-fabricated microstructure. As the majority of the pull-outs removed from the images are co-localized with the UO_2 precipitates (see Figure 22), it is possible that the exclusion of the pull-out areas leads to an underestimation of the amount of UO_2 phase. Moreover, as mentioned earlier, the size threshold imposed to discriminate the fission gas bubbles might have an impact on the area

fraction measurement of the UO_2 precipitates, despite it is expected to be small due to the small area threshold. Regarding the fission gas bubbles, their development is consistently observed within 60% of the radius in both rodlets. More scattered are the results on the periphery, where occasionally the surface is decorated with small round features that could be attributed to bubbles (see dashed circles in Fig. 12f). The systematic development of larger bubbles in the more central part of the pellet is consistent with the local higher irradiation temperature to be expected in those regions. It should be noted that at radii exceeding $r/r_0 > 0.6$, smaller bubbles not resolvable with the optical microscopy likely exists.

The discrimination of the bubbles is largely dependent on the size threshold imposed. Therefore, the absolute quantitative information in Figure 31 is not to be considered fully reliable, but the segmentation procedure captures the qualitative evolution of the bubbles along the pellet radius, giving a first insight on the fission gas behavior in U_3Si_2 fuels at low burnup for the irradiation conditions in Table 4. Advanced PIE such as SEM and TEM are required to provide a more reliable quantitative estimation of the fission gas bubbles. Those will be the objective of a future work.

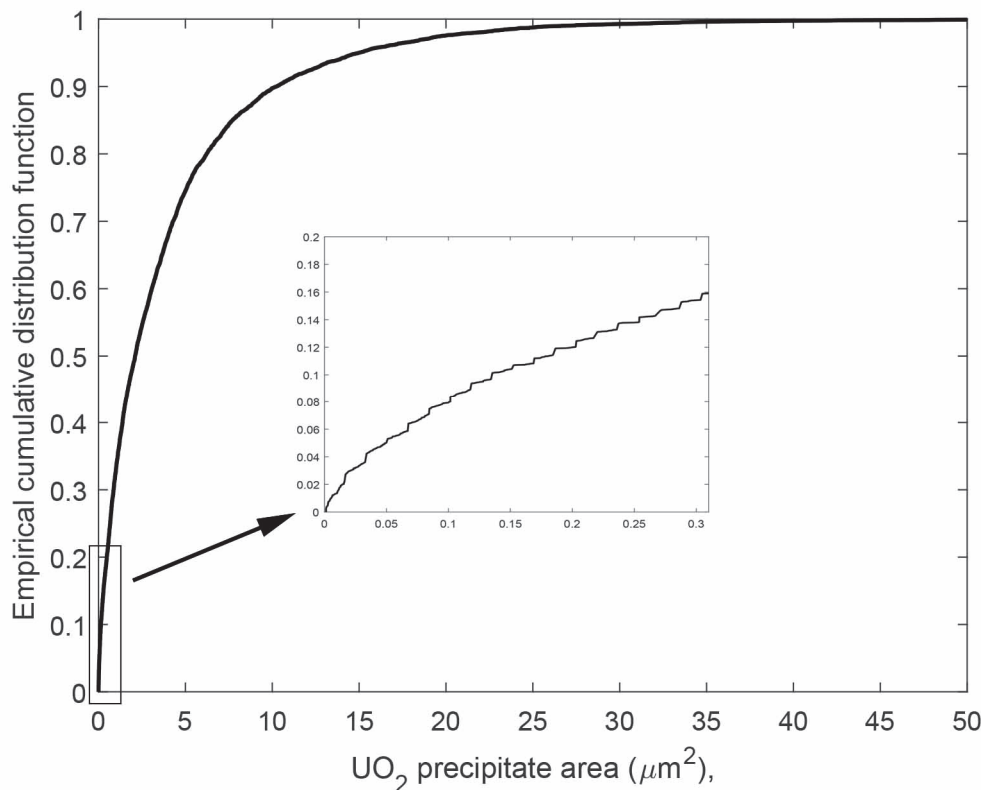


Figure 29. Empirical cumulative distribution function of the UO_2 precipitate area in the as-fabricated microstructure.

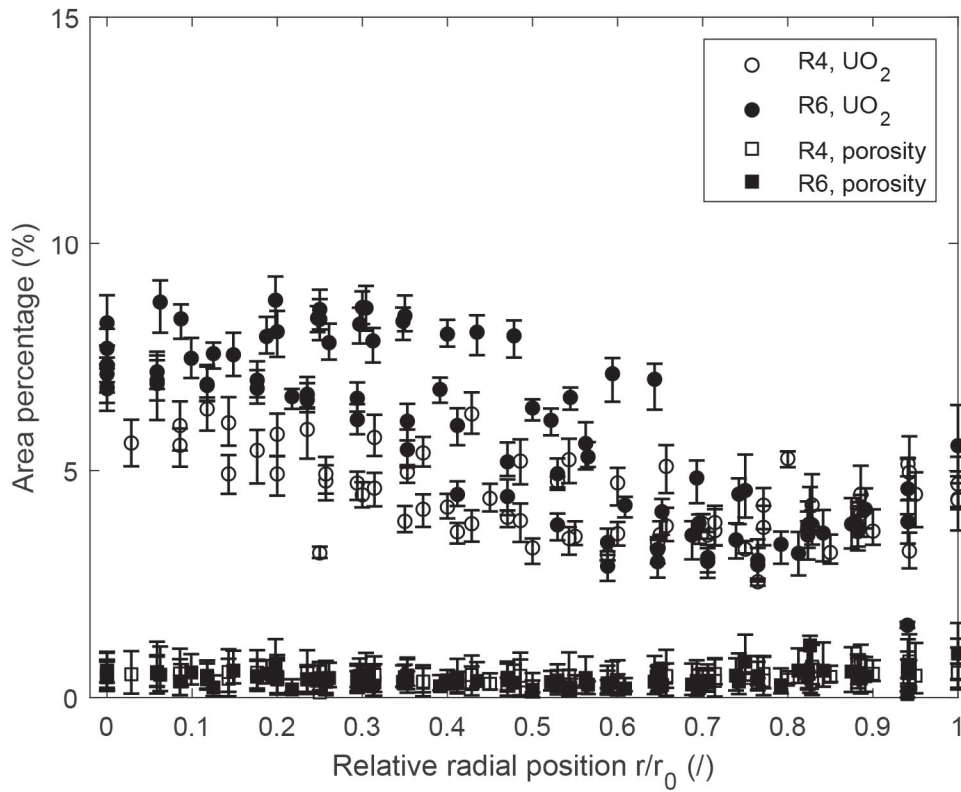


Figure 30. Radial distribution of the UO₂ precipitates and associated porosity for the two irradiated rodlets.

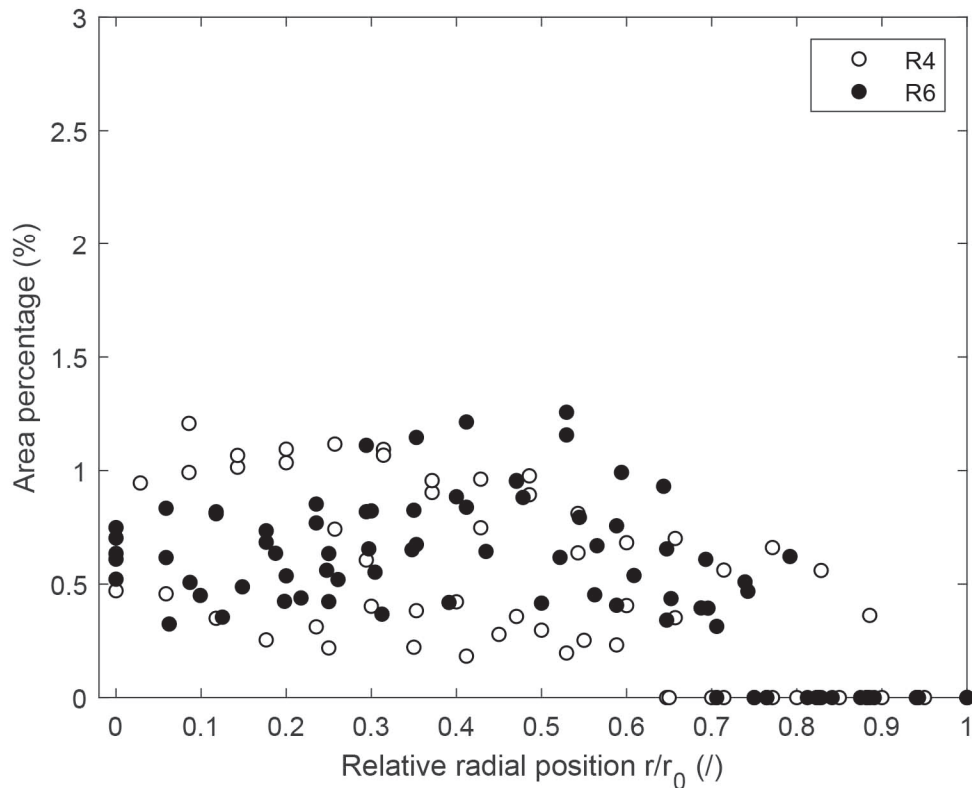


Figure 31. Radial distribution of fission gas bubbles for the two irradiated rodlets.

4.2.1 As-Fabricated Microstructure Image Analysis

The algorithm used for the segmentation of the images for the second set is depicted in Figure 32. This algorithm consists of three main steps: STEP 1 deals with the segmentation of the porosity, STEP 2 is dedicated to the segmentation of the dark UO_2 precipitates and STEP 3 deals with the segmentation of the lighter Si-rich phases. Each step is further divided in sub-routines, as shown in Figure 32.

4.2.1.1 STEP 1: porosity segmentation

The core of the porous regions can be highlighted applying a Local Binary Pattern (LBP) transformation of the original image in a 4-neighbourhood. The LBP is a type of visual descriptor used for texture classification in computer vision [52], where homogeneous dark areas appear as minima in the LBP. Small pores do not appear as local minima in the LBP due to the image noise. Those are separated based on the image histogram, as they correspond to the darkest part in the histogram. They are selected setting an adaptive threshold 50 times bigger than the minimum grey-level of the image histogram. The proportionality to the minimum grey-level is necessary to account for different brightness in the different images. In order to exclude isolated dark pixels due to noise, an additional selecting criterion has been established: if the standard deviation in a 3×3 neighborhood around the pixel does exceed a specified threshold (here set to 0.2), the pixel is considered noise and excluded. Refinement of the porosity seeds has been carried out by allowing object growing based on grey-level similarity. Adjacent pixels are added to the pore if their grey value distance is within 2.5% from the seed average grey-level value. Due to the large noise of the image, pore borders appear very irregular. This fact is quite unrealistic from a physical point of view. In order to regularize the pore borders, edge smoothing has been allowed. Adjacent pixels

are added to the pore if their contribution suppresses the irregularity of the borders. An example of the object refinement routine (STEP 1 phase B in Figure 32) is displayed in Figure 33.

4.2.1.2 STEP 2: UO₂ phase segmentation

UO₂ phase appears as dark precipitates in the BSE images. From this step on, a Gaussian filter [53] is applied to the image in order to suppress the high frequency noise, which hinders proper segmentation of the objects. Each image is segmented into 4 clusters corresponding to U₃Si₂, Si-rich phases, UO₂ and porosity (Fig. A.3) using a k-means clustering algorithm [41]. The filter dramatically improves the segmentation of both dark and light precipitates, but it smears the porosity, which is now not distinguished from the UO₂ precipitates. This issue can be corrected by assigning two cluster values (1 and 2) to the UO₂ precipitates and subtracting the porosity areas segmented during STEP 1.

4.2.1.3 STEP 3: Si-rich phase segmentation

The precipitates in lighter gray color correspond to the Si-rich phases. They are identified by cluster number 3 in Figure 34a. Residual noise or surface contamination result in detection of very small areas dispersed in the background. In order to avoid detection of noise, a cut-off areas has been set equal to 30 pixels. All the features smaller than this value are considered noise and converted to background. Another un-physical phenomenon appears from the segmentation: some pixels around the dark precipitates fall into the light precipitate cluster, as indicated by the circle in the top part of Figure 34b. It is probable that those liners are an illumination artifact occurring along the UO₂ phase boundaries, in particular considering that the precipitates are associated with irregularities in the sample surface which impact the electron beam. They can be separated from the “real” precipitates based on texture analysis. The grey-level co-occurrence matrix [54] is calculated for each pixel in cluster 3. Pixel texture score is computed as the evenly weighted average of the local texture properties contrast, correlation, energy and homogeneity [54]. An example of the texture score of the image is reported in Figure 35a. The classification in three clusters (Figure 35b) allows to isolate the illumination artifacts. These are re-assigned to the adjacent cluster iteratively proceeding from the exterior to the interior till each border is fully re-assigned. Another artifact due to the image noise is the presence of holes and concave regions inside the secondary phases (red circle on the far right in Figure 34b). Occurrence of complex concave shapes seems unphysical, it is due to the noise in the image. The uncertainty in the assignment of those regions can be treated by applying fuzzy-logic [55] in the segmentation process. The approach consists of inspecting pixels initially categorized as U₃Si₂ (cluster 4) in order to construct a transform of the original image which represents the probability of those pixels belonging to the Si-rich phase on the basis of some topological relationship between the pixel and the precipitates. For each pixel, two neighborhood of different size, i.e., two disks of radius 3 and 7 pixels, respectively, are constructed. They represent short and medium range topology around the pixel. In each neighborhood, two parameters are evaluated: (1) the number of different objects in cluster 3 that are included in the neighborhood, and (2) the amount of overlapping in the neighborhood. The first parameter is connected to the probability that the background pixel lies in the concave regions among the precipitates. The second is a measure of the proximity of the pixel to the objects. For both parameters, a linear fuzzy membership is assumed. The membership is maximum if in the pixel neighborhood there are more than three objects belonging to cluster 3 or all the neighboring pixels belongs to cluster 3. The final score selects the pixels with a high probability of lying in the concave regions of the precipitates. They are added to the object if, following addition of those pixels, the result is an object with more regular shape. The process is iterated till no regularization of the Si-rich precipitates occurs. An example of the final result of the segmentation after optimization is reported in Figure 34c.

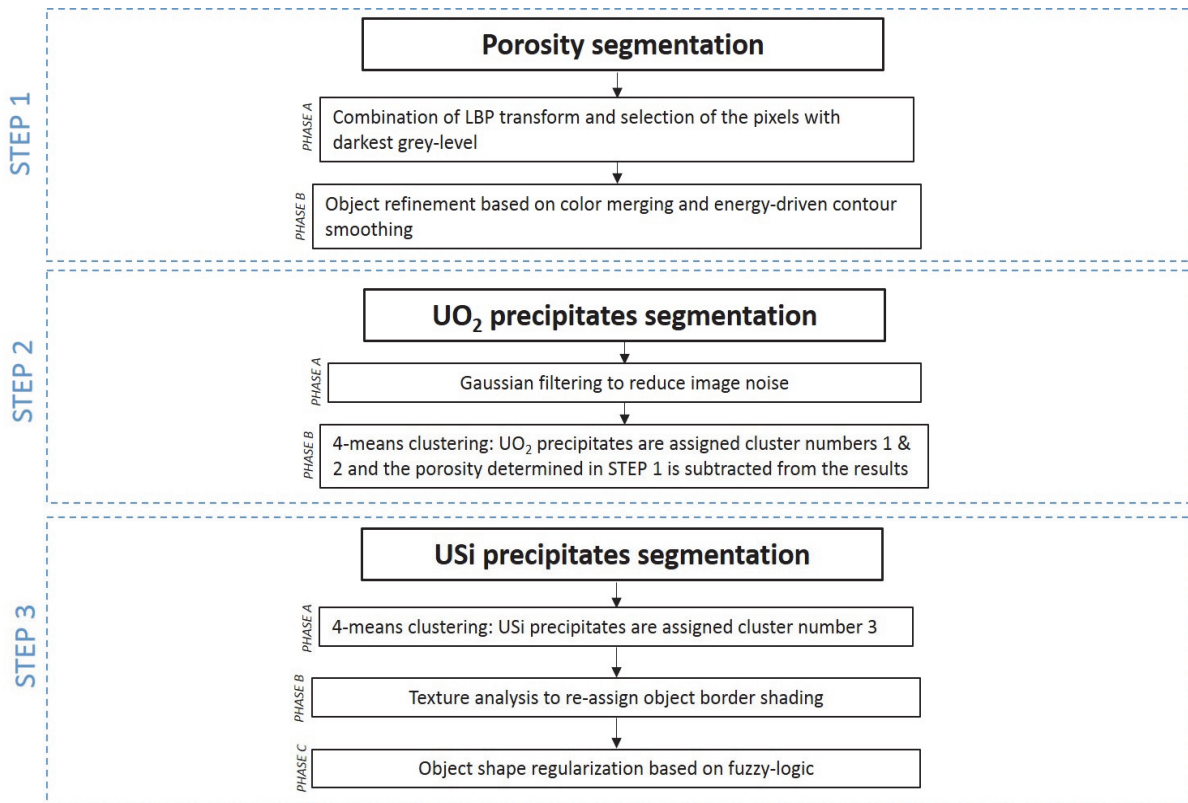


Figure 32. Algorithm scheme for the as-fabricated microstructure.

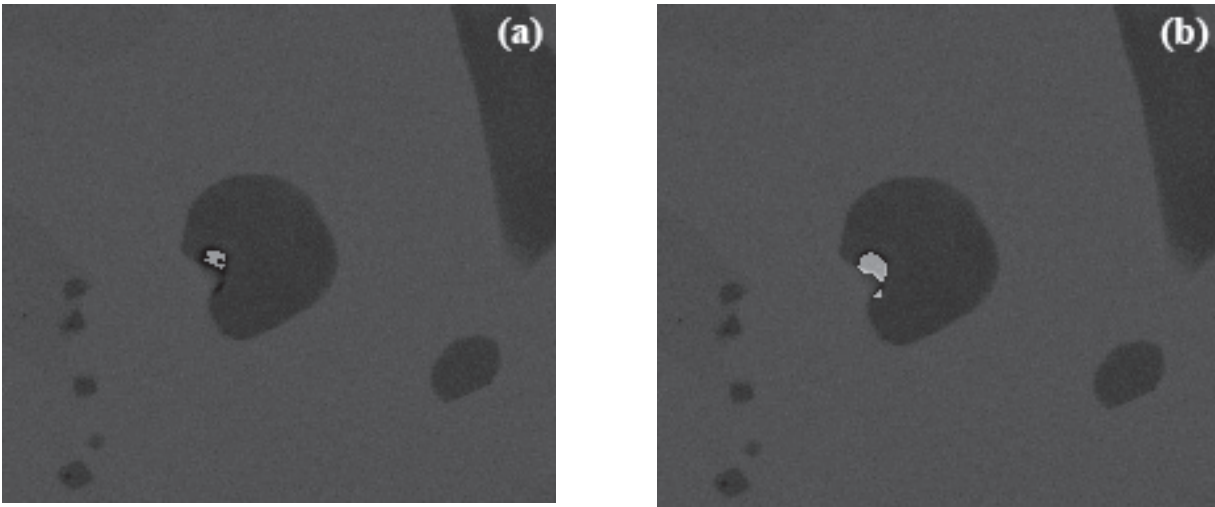


Figure 33. (a) Initial porosity segmentation, (b) pore refinement based on region merging via color-merging and edge smoothing.

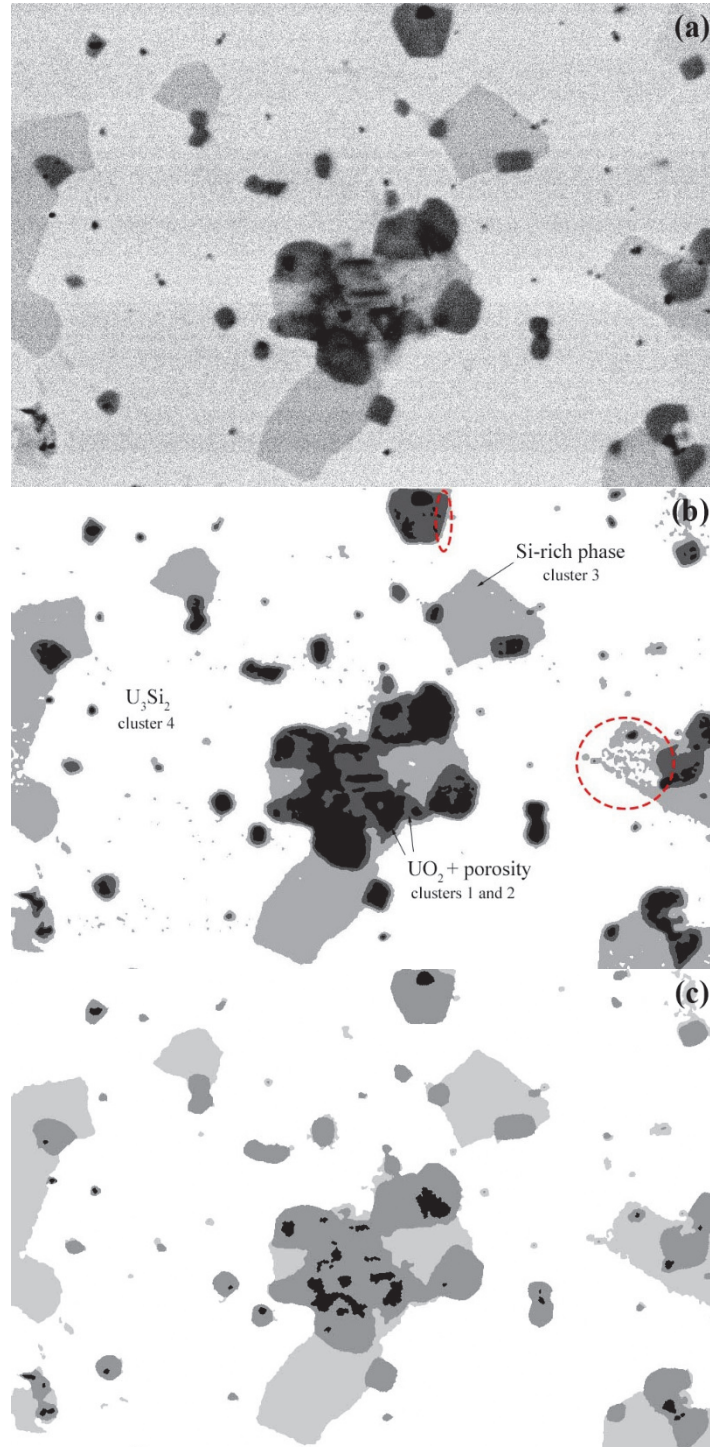


Figure 34. (a) Original BSE image, (b) initial segmentation using a k-means algorithm with 4 clusters, (c) final output of the segmentation after optimization in STEP 2 and 3.

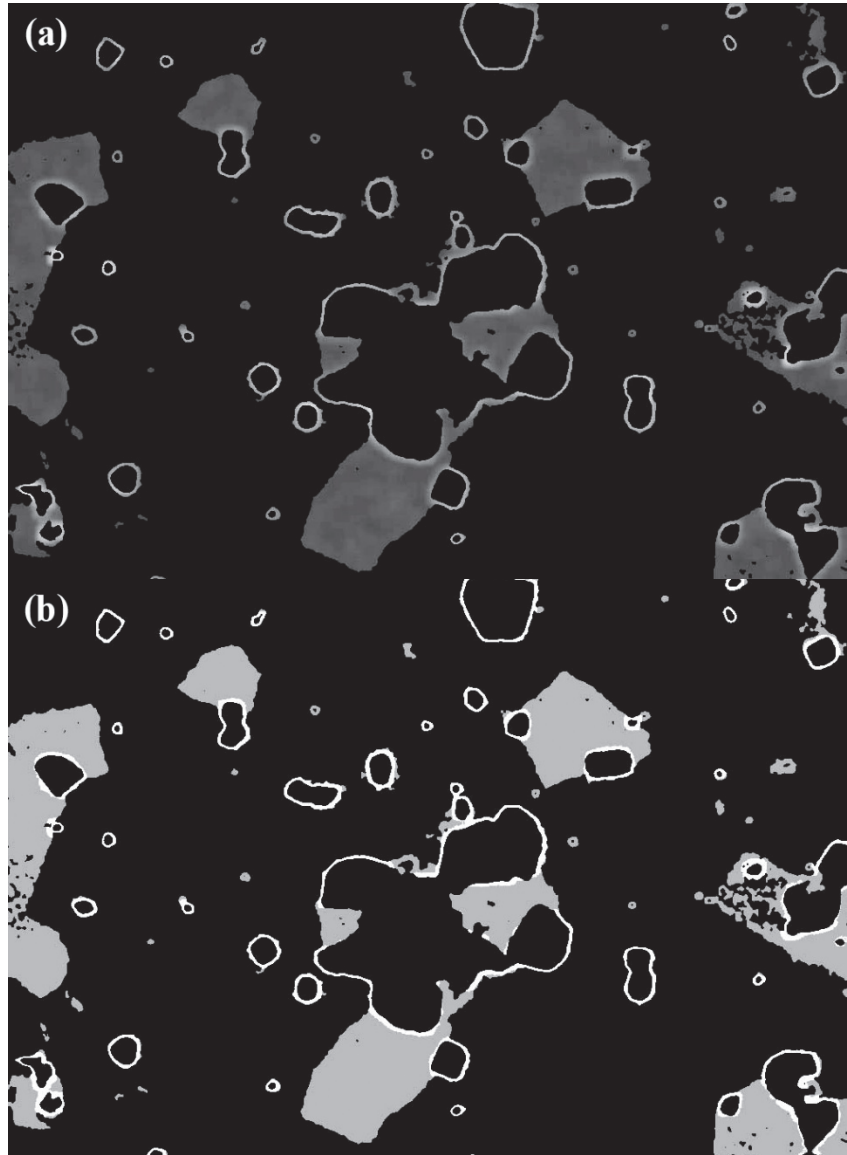


Figure 35. (a) Texture score transform of the original image, (b) Segmentation of the borders based on a 3-cluster classification of the score in (a).

4.2.2 Irradiated Microstructure Image Analysis

An overview of the algorithm scheme is reported in Figure 36.

4.2.2.1 STEP 1: UO₂ and porosity segmentation

The algorithm starts with a binarization of the image to perform a global search of the UO₂ precipitate location, exploiting the remarkable color difference between those and the background. These will represent the object seeds used in the subsequent analysis. The sample surface presents occasional pull-outs and residual scratches from the sample preparation process, which need to be excluded from the analysis. Therefore, two additional sub-steps are included to separate those features. Regarding the pull-outs, the model uses a combination of two

characteristics to identify them: first, their size is generally much larger compared to the average precipitate size, therefore, a size limit can be set. All the identified features whose area exceeds the limit (which was assumed to be $\approx 57\mu\text{m}^2$) are automatically identified as pull-outs and excluded from the counts. The second characteristic is associated with the color of the pull-outs. In the vast majority of the cases, the pull-out is associated with a region showing high brightness compared to the rest of the surface and a golden color (see Figure 23e). Those areas can be easily segmented from a transformation of the image to the YCbCr color space^a, in which these areas are better highlighted by the separation of luma and chroma information, reducing at the same time the redundancy in color information typical of the RGB color space. Including this second characteristic in the segmentation model allows to properly exclude also the vast majority of the small pull-outs. The areas identified with the pull-outs are subtracted from the total image area (see Figure 37b). Occasionally, long scratches resulting from the sample preparation could be visible on the sample surface. They can be localized from the peaks in the Hough transform [56]. The objects matching the position of the lines are removed.

Phase B consists in the separation of the porous regions internal to the objects identified in phase A using a combination of region splitting and merging [53], on the basis of the object configurations encountered. As the UO_2 precipitates are surface irregularities, the brightness within the precipitates varies with its morphology and illumination conditions. The possible configurations are the following. Case (1): the object contains three identifiable regions, a light grey part corresponding to the precipitate borders, a dark grey part corresponding to its core and the porosity (Figure 38a). Case (2): the object contains only two regions, the light precipitate part and a dark precipitate part (Figure 38b). Case (3): the object contains only two regions, the light precipitate part and the porosity (Figure 38c). Each object is initially binarized, splitting the object into a light part and a dark part. The light part is assigned to the precipitate area, the other is named "guess" region and further analyzed. In the guess region a decision tree is constructed based on the grey-level range. If the local range exceeds a pre-determined threshold, the object belongs to case (1). The guess region is further split into dark and light part. The darker part is assigned to the porosity, whereas the rest is merged back to the area initially assigned as precipitate area. If the local range of the guess region does not exceed the threshold, the relative distance of the mean gray level in the guess region and the precipitate area is evaluated to decide if it is case (2) or (3). If the normalized distance exceeds the pre-determined threshold T , the object belongs to case (3), otherwise it belongs to case (2). The logical sub-routine is summarized in Figure 39. As the pre-determined threshold influences whether the regions are identified as porosity or precipitates, an estimation of the error related to the model parameter is provided by varying it from a minimum value to its double. In particular, the analysis has been carried out assuming that the distance between the mean grey-levels in the two zones should span over 30% till 60%. The advantage of using a local approach is the possibility of dealing with variations in the brightness of the objects due to shading effects within the optical microscopy field of view. In the last phase, a refinement of the precipitates is performed implementing a region growing algorithm that combines edge-based and color-based object segmentation. First, the closed edges from the Canny edge transform [53] of the image are selected and compared to the object seeds positions from phase A. If the seed position matches

^a Study shows that human eyes are more sensitive to luminance than to chrominance. The YCbCr space conversion is a useful tool used to separate the two components. The Y channel (luminance) contains information similar to the grey-level conversion of the color image, but the combination with the chroma channels Cb and Cr allows easier identification of the interested areas, which can be distinguished from the background also based on color.

the edge location, the seed is expanded till the boundary is encountered. Other features do not present sharp closed edges, and the described approach cannot be used. For those, the region growing is performed based on the color distance map of the surrounding area. For each seed, the color marker is calculated averaging the color of the precipitate in the L^*a^*b color space (excluding the porosity, if present). Adjacent pixels are added to the precipitate if their color distance is within 10% from the seed average.

4.2.2.2 STEP 2: Fission gas bubbles segmentation

The fission gas bubbles present similarity of color and common morphological characteristics, namely a small size and an almost circular shape. It was found that the bubbles could be segmented best by applying a k-means segmentation approach using four clusters and selecting only the objects belonging to the two central clusters (rejecting the mid grey-level values of the bubbles) with high value of solidity and with Euler number equal to one (approximating the circular shape). An example of the resulting microstructure segmentation is displayed in Figure 37b.

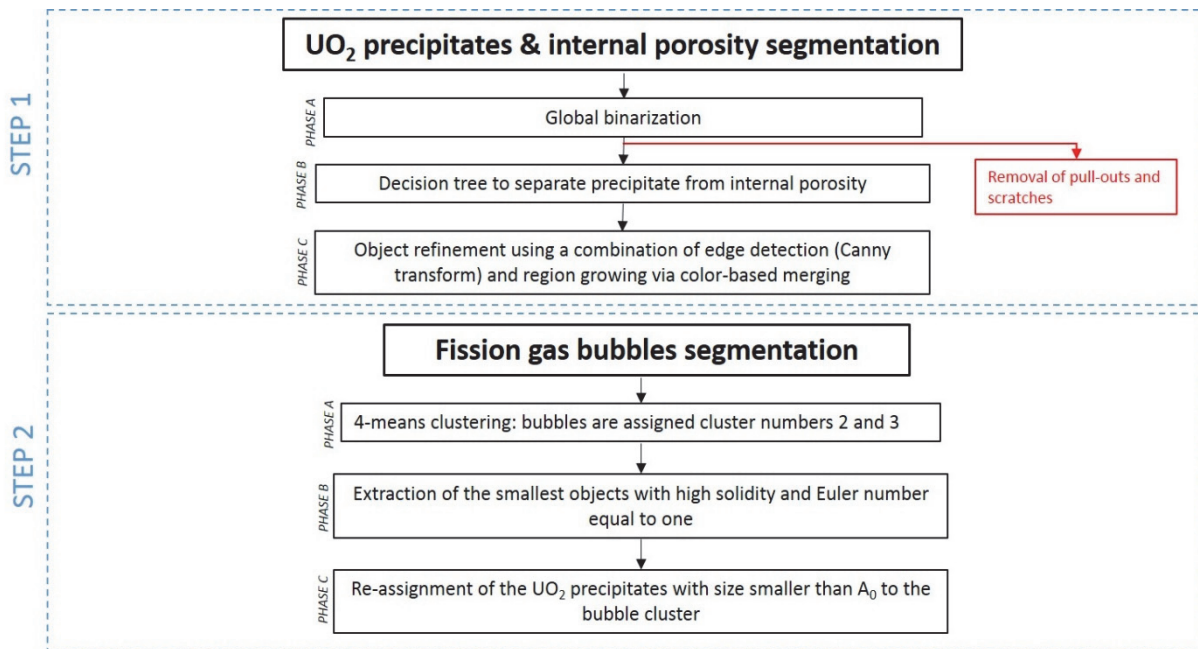


Figure 36. Algorithm scheme for the irradiated microstructure.

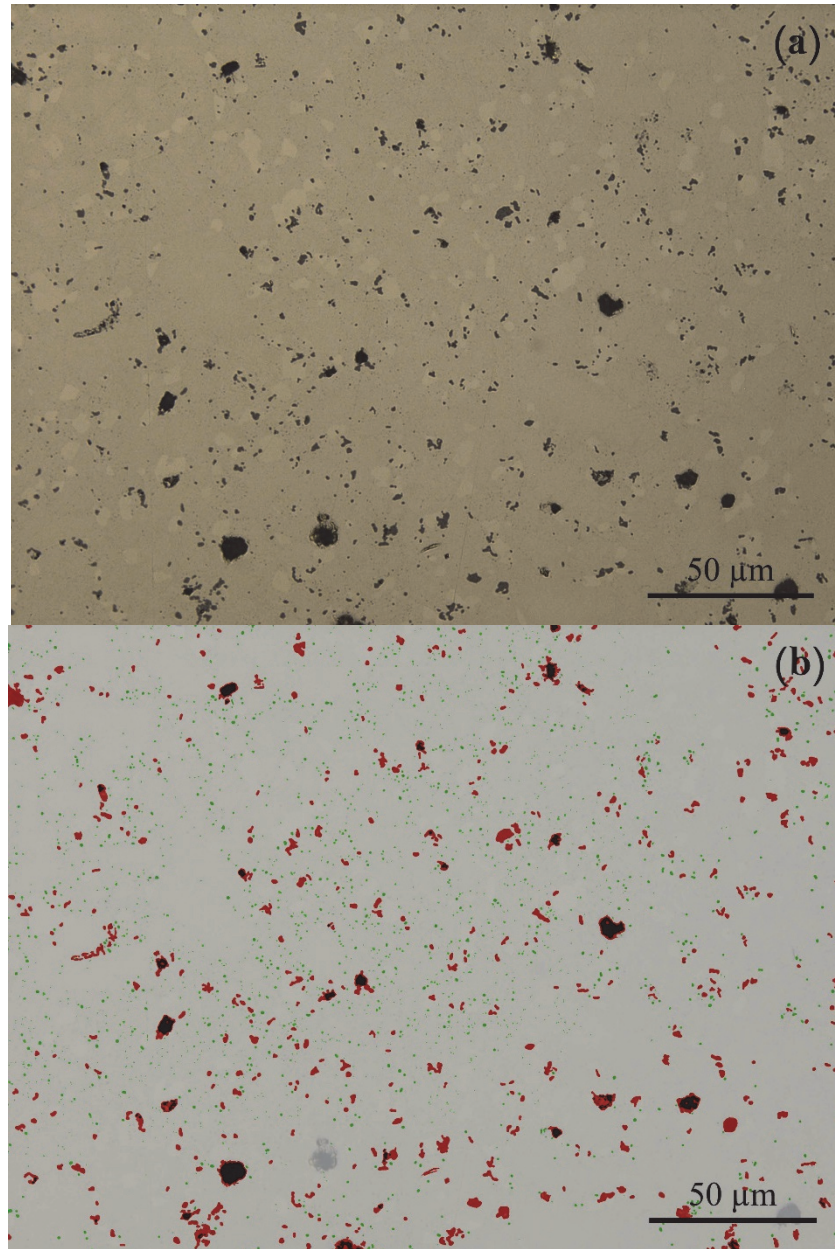


Figure 37. (a) Original image, (b) Segmentation results overlaid to the original image in (a). Red color corresponds to the UO₂ precipitates, black color to the porosity and green color to the fission gas bubbles.

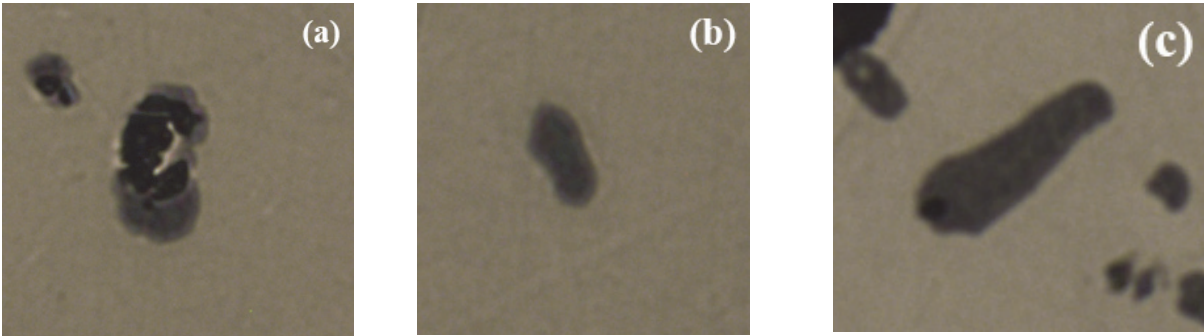


Figure 38. Examples of different configurations of UO₂ precipitates and associated porosity encountered in the images: (a) Case 1, (b) Case 2, (c) Case 3.

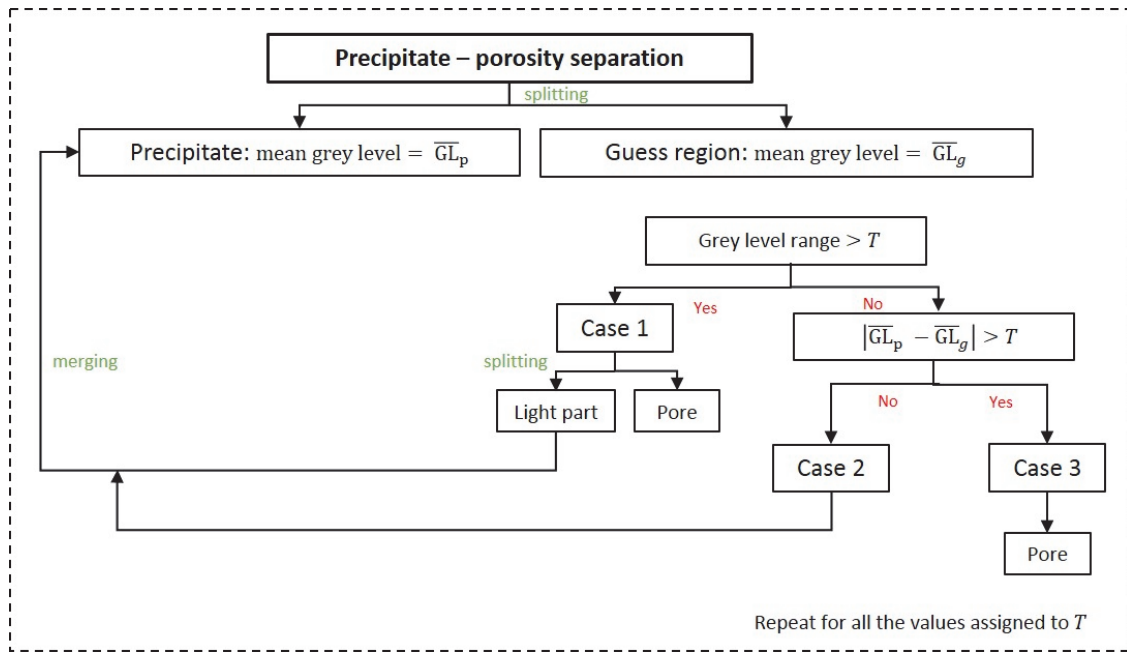


Figure 39. Logic tree to separate the UO₂ precipitates from the internal porosity performed in STEP 1 phase B.

5. Other ATF-1 PIE

This report has focused on the 2 completed exams performed for industrial partners. There are 5 other ATF-1 capsules at varying steps in the PIE process also undergoing PIE. This section will summarize the current state of these capsules.

5.1 ATF-18 ORNL LOCA FCA-L3

The ATF-18 capsule contained an early variation of a FeCrAl alloy called C35MN, which is Fe-13Cr-5Al with minor additions of Mo and Nb [57]. The cladding was filled with UO₂ pellets and irradiated to approximately 10 GWd/mtU burnup. The rodlet in ATF-18 was designated ORNL LOCA FCA-L3. The intent of this irradiation was to create irradiated samples for the Oak Ridge National Laboratory (ORNL) Severe Accident Test Station [58,59]. The tubes used in this irradiation were created by gun drilling not drawing. This creates a non-prototypic microstructure in the tube, but this difference is inconsequential when studying fuel-cladding interaction. However, it was found that welding this particular configuration was difficult. Consequently, the hermeticity of the welds was suspect after irradiation. The gun drilled nature of the tube also raises suspicions that the tube itself may be vulnerable to brittle micro-cracking. This capsule was checked on GASR prior to disassembling the capsule, and fission gas was detected in the capsule. The free volume measured by GASR was also near the free volume of the capsule and the rodlet that was estimated from drawings. The fission gas release for the fuel was found to be 0.35% which is in-line with expectations from the Vitanza curve for this fuel [34]. No obvious flaw has been detected in visual exams or neutron radiography (see Figure 40 for examples). There was some measurable change in cladding diameter as seen in Figure 41. The cladding measures greater than the maximum reported diameter in the as-built documentation of 9392 μm , so there may be some irradiation or thermal induced cladding strain. Currently, this rodlet is in storage waiting for shipment to ORNL. Although with the rodlet being breached, it may not be an ideal candidate for use in the Sever Accident Test Station.

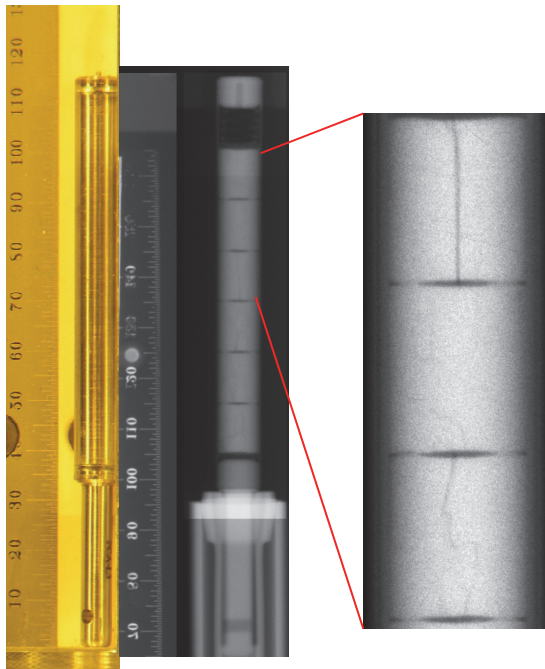


Figure 40. Visual Examination and neutron radiography of the ORNL LOCA FCA-L3 rodlet with a neutron radiography detail that shows cracking in the UO₂ pellets

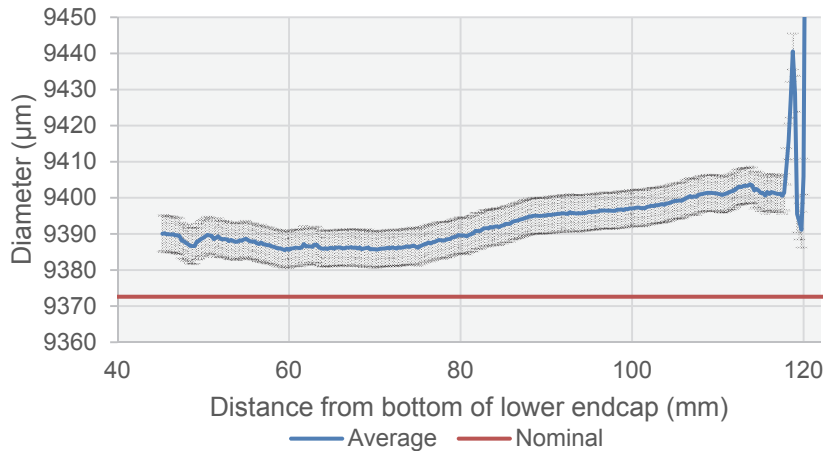


Figure 41. Dimensional inspection of the FeCrAl rodlet from ATF-18 (ORNL LOCA FCA-L3)

5.2 ATF-06, ATF-08, ATF-45, ATF-73

Four additional ATF-1 capsules were received at HFEF from ATR in April 2018. Thermal neutron radiography of these capsules is shown in Figure 42. The ATF-06 capsule is labeled 1 in Figure 42 and contains UO_2 clad with Alloy-33 a commercial FeCrAl alloy. The ATF-08 capsule is labeled 2 in Figure 42 and contains UO_2 clad with APMT a commercial FeCrAl alloy. The ATF-45 capsule is labeled 3 in Figure 42 and contains U_3Si_5 clad with Kanthal AF a commercial FeCrAl alloy. The ATF-73 capsule, labeled 4 in Figure 42, contains a fuel-cladding interaction test. This capsule contains discs of UO_2 against discs of different FeCrAl test alloys fabricated by ORNL. This capsule and rodlet is essentially several diffusion couple tests.

Capsule visual inspections, capsule neutron radiography, and capsule gamma spectrometry have been performed on these capsules. These capsules are currently waiting to be punctured on the GASR system to check rodlet integrity prior to capsule disassembly. This extra step is being performed on these FeCrAl alloy rodlets based on the loss of hermeticity in the ATF-18 rodlet.

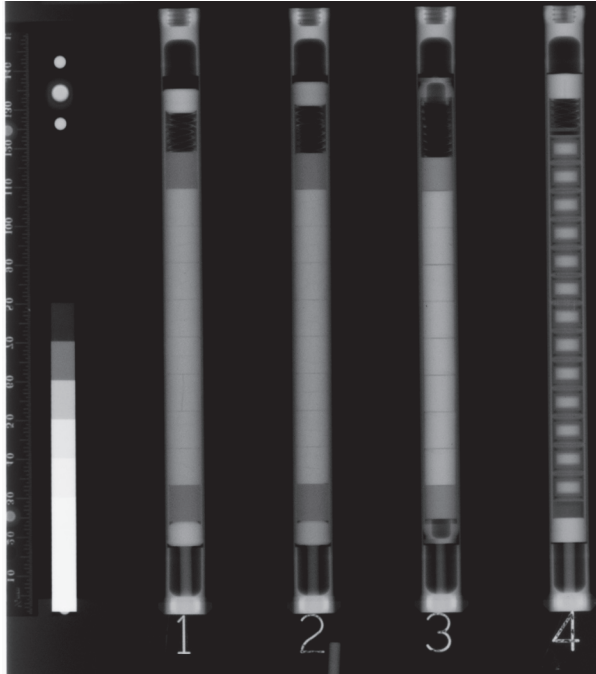


Figure 42. Neutron radiography of ATF-1 capsules, from left to right ATF-06, ATF-08, ATF.45, ATF-73

6. CONCLUSIONS

This report summarizes the PIE performed on the currently available rodlets from the ATF-1 irradiation tests. These irradiation tests investigated a variety of different concepts.

Both non-destructive and destructive PIE have been carried out on $\text{UO}_2\text{-SiC}$ and $\text{UO}_2\text{-diamond}$ composites, which have been proposed as ATF candidates. The dimensional measurements did not show abnormal cladding strain in any of the analyzed rods, meaning that no excessive swelling of the fuel pellets occurred during irradiation. The results of the $\text{UO}_2\text{-SiC}$ at low burnup have highlighted a general trend to enhanced cracking compared to the UO_2 rodlet used as comparison for performance assessment. In addition, instability of the SiC whiskers at irradiation temperatures exceeding $1300\text{ }^\circ\text{C}$ has been observed. The microstructure of the $\text{UO}_2\text{-diamond}$ pellets has been severely damaged during the irradiation, displaying extensive cracking across the full pellets. The enhanced fission gas release measured compared to the expected value from the Vitanza curve is most likely related to the pellet fracturing. Also irregular local ^{137}Cs signal spikes along the fuel stack suggest some migration of the fission products along the cracked fuel matrix. The results of the PIE reveal a poor performance of the two composites compared to UO_2 fuel, challenging their deployment as accident tolerant fuels.

Non-destructive and destructive PIE have been carried out on U_3Si_2 fuels in order to assess its performance at LWR irradiation temperatures and burnup below 20 GWd/tHM . Microindentation tests have shown a minor hardening of the fuel matrix related to accumulation of fission products and radiation damage. The data revealed how both the FGR and swelling at low burnup remain limited. Development of bubbles visible with optical microscope is obvious in most of the pellet, but more advanced imaging tools (e.g., SEM) are required for accurate determination of the porosity value across the pellet radius. Detailed microstructural investigation employing SEM and TEM are foreseen in future work to complement the engineering-scale examinations here reported.

The overall results of the PIE reveal good performance of the silicide pellets under normal operating conditions and at low burnup. Further irradiation tests are ongoing to evaluate the performance of U_3Si_2 at high burnup.

ATF-1 PIE continues on several other ATF-1 capsules that are in various stages of PIE. The results of PIE will periodically be published, and further updates on the status of ATF-1 PIE will be forthcoming on the additional capsules that have begun PIE in HFEF.

7. REFERENCES

- [1] J. Carmack, F. Goldner, Forward for special JNM issue on accident tolerant fuels for LWRs, *J. Nucl. Mater.* 448 (2014) 373.
- [2] S.M. Bragg-Sitton, M. Todosow, R. Montgomery, C.R. Stanek, R. Montgomery, W.J. Carmack, Metrics for the Technical Performance Evaluation of Light Water Reactor Accident-Tolerant Fuel, *Nucl. Technol.* 195 (2016) 111–123.
- [3] Nuclear Energy Agency Organisation for Economic Co-operation and Development, Nuclear Fuel Safety Criteria Technical Review, 2012.
- [4] K.A. Terrani, D. W., L.J. Ott, R.O. Montgomery, The effect of fuel thermal conductivity on the behavior of LWR cores during loss-of-coolant accidents, *J. Nucl. Mater.* 448 (2014) 512–519.
- [5] W. Zhou, W. Zhou, Enhanced thermal conductivity accident tolerant fuels for improved reactor safety – A comprehensive review, *Ann. Nucl. Energy.* 119 (2018) 66–86. doi:10.1016/j.anucene.2018.04.040.
- [6] N.E. Todreas, M.S. Kazimi, Nuclear Systems I - Thermal Hydraulic Fundamentals, in: Taylor & Francis, 1990: p. 317.
- [7] P. Weimar, F. Thümmler, H. Bumm, UO₂-cermets with idealized structure by particle coating and isostatic hot pressing, *J. Nucl. Mater.* 31 (1969) 215–225.
- [8] A.F.S. LLC, Phase 1A Final Report for the AREVA Team Enhanced Accident Tolerant Fuels Concepts, 2015.
- [9] S. Yeo, E. McKenna, R. Baney, G. Subhash, J. Tulenko, Enhanced thermal conductivity of uranium dioxide–silicon carbide composite fuel pellets prepared by Spark Plasma Sintering (SPS), *J. Nucl. Mater.* 433 (2013) 66–73. doi:10.1016/J.JNUCMAT.2012.09.015.
- [10] G.A. Slack, Nonmetallic crystals with high thermal conductivity, *J. Phys. Chem. Solids.* 34 (1973) 321–335.
- [11] M.I. Landstrass, D.M. Fleetwood, Total dose radiation hardness of diamond-based silicon-on-insulator structures, *Appl. Phys. Lett.* 56 (1990) 2316–2318.
- [12] Z. Chen, G. Subhash, J.S. Tulenko, Spark plasma sintering of diamond-reinforced uranium dioxide composite fuel pellets, *Nucl. Eng. Des.* 294 (2015) 52–59. doi:10.1016/J.NUCENGDES.2015.08.021.
- [13] I. Charit, Accident Tolerant Nuclear Fuels and Cladding Materials, *J. Miner. Met. Mater. Soc.* 70 (2018) 173–175.
- [14] Y.S. Kim, G.L. Hofman, J. Rest, A.B. Robinson, Temperature and dose dependence of fission-gas-bubble swelling in U₃Si₂, *J. Nucl. Mater.* 389 (2009) 443–449.
- [15] Y.S. Kim, 3.14 - Uranium Intermetallic Fuels (U–Al, U–Si, U–Mo), in: R.J.M. Konings (Ed.), *Compr. Nucl. Mater.*, Elsevier, 2012: pp. 401–411.
- [16] J. Rest, A model for fission-gas-bubble behavior in amorphous uranium silicide compounds, *J. Nucl. Mater.* 325 (2004) 107–117.
- [17] R.C. Birtcher, J.W. Richardson, M.H. Mueller, Amorphization of U₃Si₂ by ion or neutron irradiation, *J. Nucl. Mater.* 230 (1996) 158–163.
- [18] G. Ruggirello, H. Calabroni, M. Sanchez, G. Hofman, Post-irradiation examination of U₃Si₆-Al fuel element manufactured and irradiated in Argentina, in: *Proc. 2002 RERTR Meet.*, Vienna, Austria, 2002.

- [19] M.R. Finlay, G.L. Hofman, J.L. Snelgrove, Irradiation behaviour of uranium silicide compounds, *J. Nucl. Mater.* 325 (2004) 118–128.
- [20] R.C. Birtcher, L.M. Wang, Stability of Uranium Silicides During High Energy Ion Irradiation, *MRS Proc.* 235 (1991) 467.
- [21] Y. Miao, J. Harp, K. Mo, Y.S. Kim, S. Zhu, A.M. Yacout, Microstructure investigations of U₃Si₂ implanted by high-energy Xe ions at 600 °C, *J. Nucl. Mater.* 503 (2018) 314–322. doi:10.1016/J.JNUCMAT.2018.02.031.
- [22] Y. Miao, J. Harp, K. Mo, S. Bhattacharya, P. Baldo, A.M. Yacout, Short Communication on “In-situ TEM ion irradiation investigations on U₃Si₂ at LWR temperatures,” *J. Nucl. Mater.* (2017). doi:10.1016/j.jnucmat.2016.11.020.
- [23] Y. Miao, J. Harp, K. Mo, S. Zhu, T. Yao, J. Lian, A.M. Yacout, Bubble morphology in U₃Si₂ implanted by high-energy Xe ions at 300 °C, *J. Nucl. Mater.* 495 (2017) 146–153. doi:10.1016/J.JNUCMAT.2017.07.066.
- [24] T. Yao, B. Gong, L. He, J. Harp, M. Tonks, J. Lian, Radiation-induced grain subdivision and bubble formation in U₃Si₂ at LWR temperature, *J. Nucl. Mater.* 498 (2018) 169–175. doi:10.1016/J.JNUCMAT.2017.10.027.
- [25] J.M. Harp, P.A. Lessing, R.E. Hoggan, Uranium silicide pellet fabrication by powder metallurgy for accident tolerant fuel evaluation and irradiation, *J. Nucl. Mater.* 466 (2015) 728–738. doi:10.1016/j.jnucmat.2015.06.027.
- [26] R.E. Hoggan, K.R. Tolman, F. Cappia, A.R. Wagner, J.M. Harp, Grain Size and Phase Purity Characterization of U₃Si₂ Pellet Fuel, *J. Nucl. Mater.* under review.
- [27] J. Carmack, F. Goldner, S.M. Bragg-Sitton, L.L. Snead, Overview of the U.S. DOE Accident Tolerant Fuel Development Program, in: *TopFuel 2013*, 2013.
- [28] K.E. Barrett, K.D. Ellis, C.R. Glass, G.A. Roth, M.P. Teague, J. Johns, Critical processes and parameters in the development of accident tolerant fuels drop-in capsule irradiation tests, *Nucl. Eng. Des.* 294 (2015) 38–51. doi:10.1016/J.NUCENGDES.2015.07.074.
- [29] G.M. Core, B.J. Curnutt, C. Hale, Accident Tolerant Fuels Series 1 (ATF-1) Irradiation Testing FY 2017 Status Report, Idaho Natl. Lab. Rep. (n.d.) INL/EXT-17-43220.
- [30] A.E. Craft, D.M. Wachs, M.A. Okuniewski, D.L. Chichester, W.J. Williams, G.C. Papaioannou, A.T. Smolinski, Neutron Radiography of Irradiated Nuclear Fuel at Idaho National Laboratory, *Phys. Procedia.* 69 (2015) 483–490. doi:10.1016/J.PHPRO.2015.07.068.
- [31] J.M. Harp, P.A. Demkowicz, P.L. Winston, J.W. Sterbentz, An analysis of nuclear fuel burnup in the AGR-1 TRISO fuel experiment using gamma spectrometry, mass spectrometry, and computational simulation techniques, *Nucl. Eng. Des.* 278 (2014) 395–405. doi:10.1016/j.nucengdes.2014.07.041.
- [32] D.A. Sell, C.E. Baily, T.J. Malewitz, P.G. Medvedev, D.L. Porter, B.A. Hilton, HOT CELL SYSTEM FOR DETERMINING FISSION GAS RETENTION IN METALLIC FUELS, in: United States, 2016. <https://www.osti.gov/servlets/purl/1367840>.
- [33] W.J. Maeck, R.P. Larsen, J.E. Rein, Burnup Determination for Fast Reactor Fuels: A Review and Status of the Nuclear Data and Analytical Chemistry Methodology Requirements, U.S. At. Energy Comm. TID-26209 (1973).
- [34] C. Vitanza, E. Kolstad, U. Graziani, Fission gas release from UO₂ pellet fuel at high burn-up, in: *Proc. Am. Nucl. Soc. Top. Meet. Light Water React. Fuel Perform.*, 1979. https://inis.iaea.org/search/search.aspx?orig_q=RN:11544784 (accessed April 24, 2018).

- [35] M.B. Chadwick, M. Herman, P. Obložinský, M.E. Dunn, Y. Danon, A.C. Kahler, D.L. Smith, B. Pritychenko, G. Arbanas, R. Arcilla, R. Brewer, D.A. Brown, R. Capote, A.D. Carlson, Y.S. Cho, H. Derrien, K. Guber, G.M. Hale, S. Hoblit, S. Holloway, T.D. Johnson, T. Kawano, B.C. Kiedrowski, H. Kim, S. Kunieda, N.M. Larson, L. Leal, J.P. Lestone, R.C. Little, E.A. McCutchan, R.E. MacFarlane, M. MacInnes, C.M. Mattoon, R.D. McKnight, S.F. Mughabghab, G.P.A. Nobre, G. Palmiotti, A. Palumbo, M.T. Pigni, V.G. Pronyaev, R.O. Sayer, A.A. Sonzogni, N.C. Summers, P. Talou, I.J. Thompson, A. Trkov, R.L. Vogt, S.C. van der Marck, A. Wallner, M.C. White, D. Wiarda, P.G. Young, ENDF/B-VII.1 Nuclear Data for Science and Technology: Cross Sections, Covariances, Fission Product Yields and Decay Data, Nucl. Data Sheets. 112 (2011) 2887–2996. doi:10.1016/J.NDS.2011.11.002.
- [36] R.J. White, The development of grain-face porosity in irradiated oxide fuel, *J. Nucl. Mater.* 325 (2004) 61–77.
- [37] J. Braun, C. Guéneau, T. Alpettaz, C. Sauder, E. Brackx, R. Domenger, S. Gossé, F. Balbaud-Célérier, Chemical compatibility between UO₂ fuel and SiC cladding for LWRs. Application to ATF (Accident-Tolerant Fuels), *J. Nucl. Mater.* 487 (2017) 380–395. doi:https://doi.org/10.1016/j.jnucmat.2017.02.031.
- [38] A.G. Evans, The role of inclusions in the fracture of ceramic materials, *J. Mater. Sci.* 9 (1974) 1145–1152.
- [39] S.R. Pillai, S. Anthonysamy, P.K. Prakashan, R. Ranganathan, P.R.V. Rao, C.K. Mathews, Carburization of stainless steel clad by uranium-plutonium carbide fuel, *J. Nucl. Mater.* 167 (1989) 105–109.
- [40] P. Chiotti, W. Robinson, M. Kanno, Thermodynamic properties of uranium oxycarbides, *J. Less-Common Met.* 10 (1966) 273–289.
- [41] A.K. Jain, Data clustering: 50 years beyond K-means, *Pattern Recognit. Lett.* 31 (2010) 651–666. doi:https://doi.org/10.1016/j.patrec.2009.09.011.
- [42] N. Otsu, A threshold selection method from gray-level histograms, *IEEE Trans. Syst. Man. Cybern.* 9 (1979) 62–66.
- [43] T.F. Chan, L.A. Vese, Active contours without edges, *IEEE Trans. Image Process.* 10 (2001) 266–277. doi:10.1109/83.902291.
- [44] S. Nagabhushana, Introduction, in: *Comput. Vis. Image Process.*, First Edit, New Age International Publisher, 2005: pp. 21–23.
- [45] J. Spino, D. Papaioannou, I. Ray, Rim formation and fission gas behaviour: some structure remarks, in: *Fission Gas Behav. Light Water React. Fuels*, Cadarache\mbox{, } France, 2000: pp. 247–268.
- [46] J.M. Harp, P.A. Demkowicz, Investigation of the Feasibility of Utilizing Gamma Emission Computed Tomography in Evaluating Fission Product Migration in Irradiated TRISO Fuel Experiments, in: *Int. Top. Meet. High Temp. React. Technol. (HTR 2014)*, WeiHai, China, 2014.
- [47] J.D. Hunn, C.A. Baldwin, T.J. Gerczak, F.C. Montgomery, R.N. Morris, C.M. Silva, P.A. Demkowicz, J.M. Harp, S.A. Ploger, Detection and analysis of particles with failed SiC in AGR-1 fuel compacts, *Nucl. Eng. Des.* (2015). doi:10.1016/j.nucengdes.2015.12.011.
- [48] J.M. Harp, H.J.M. Chichester, L. Capriotti, Postirradiation examination results of several metallic fuel alloys and forms from low burnup AFC irradiations, *J. Nucl. Mater.* 509 (2018) 377–391. doi:10.1016/J.JNUCMAT.2018.07.003.
- [49] Standard method for Vickers indentation hardness of advanced ceramics, (1999).

- [50] J. Spino, J. Cobos-Sabate, F. Rousseau, Room-temperature microindentation behaviour of LWR-fuels, part 1: fuel microhardness, *J. Nucl. Mater.* 322 (2003) 204–216. doi:[https://doi.org/10.1016/S0022-3115\(03\)00328-3](https://doi.org/10.1016/S0022-3115(03)00328-3).
- [51] M. Oguma, Cracking and relocation behavior of nuclear fuel pellets during rise to power, *Nucl. Eng. Des.* 76 (1983) 35–45.
- [52] T. Ojala, M. Pietikäinen, D. Harwood, A comparative study of texture measures with classification based on featured distributions, *Pattern Recognit.* 29 (1996) 51–59. doi:[https://doi.org/10.1016/0031-3203\(95\)00067-4](https://doi.org/10.1016/0031-3203(95)00067-4).
- [53] M. Sonka, V. Hlavac, R. Boyle, Image pre-processing, in: *Image Process. Anal. Mach. Vis.*, 2015: pp. 144–147.
- [54] L. Shapiro, G. Stockman, Texture, in: *Comput. Vis.*, 2000: pp. 240–242.
- [55] M. Sonka, V. Hlavac, R. Boyle, Segmentation II, in: *Image Process. Anal. Mach. Vis.*, 2015: pp. 280–288.
- [56] M. Sonka, V. Hlavac, R. Boyle, Segmentation I, in: *Image Process. Anal. Mach. Vis.*, 2015: pp. 220–229.
- [57] Y. Yamamoto, B.A. Pint, K.A. Terrani, K.G. Field, Y. Yang, L.L. Snead, Development and property evaluation of nuclear grade wrought FeCrAl fuel cladding for light water reactors, *J. Nucl. Mater.* 467 (2015) 703–716. doi:[10.1016/J.JNUCMAT.2015.10.019](https://doi.org/10.1016/J.JNUCMAT.2015.10.019).
- [58] K.D. Linton, Z.M. Burns, K.A. Terrani, Y. Yan, Hot Cell Installation and Demonstration of the Severe Accident Test Station, ORNL Report, ORNL/SPR-2017/434, United States, 2017. doi:[10.2172/1394377](https://doi.org/10.2172/1394377).
- [59] K.G. Field, J. Harp, G. Core, K. Linton, Status of Wrought FeCrAl-UO₂ Capsules Irradiated in the Advanced Test Reactor, ORNL Report, ORNL/TM-2017/366, United States, 2017. doi:[10.2172/1376535](https://doi.org/10.2172/1376535).